Fe-based superconductors: an angle-resolved photoemission spectroscopy perspective

IOP PUBLISHING REPORTS ON PROGRESS IN PHYSICS

Rep. Prog. Phys. **74** (2011) 124512 (25pp) doi:10.1088/0034-4885/74/12/124512

Fe-based superconductors: an angle-resolved photoemission spectroscopy perspective

P Richard[1], T Sato[2,3], K Nakayama[2], T Takahashi[2,4] and H Ding[1]

[1] Beijing National Laboratory for Condensed Matter Physics, and Institute of Physics, Chinese Academy of Sciences, Beijing 100190, People's Republic of China
[2] Department of Physics, Tohoku University, Sendai 980-8578, Japan
[3] TRiP, Japan Science and Technology Agency (JST), Kawaguchi 332-0012, Japan
[4] WPI Research Center, Advanced Institute for Materials Research, Tohoku University, Sendai 980-8577, Japan

E-mail: p.richard@iphy.ac.cn

Received 26 July 2011, in final form 25 October 2011
Published 25 November 2011
Online at stacks.iop.org/RoPP/74/124512

Abstract
Angle-resolved photoemission spectroscopy allows direct visualization and experimental determination of the electronic structure of crystals in the momentum space, including the precise characterization of the Fermi surface and the superconducting order parameter. It is thus particularly suited for investigating multi-band systems such as the Fe-based superconductors. In this review, we cover several aspects of these recently discovered materials that have been addressed by this technique, with a special emphasis on their superconducting gap and their Fermi surface topology. We provide sufficient experimental evidence to support the reliability and the consistency of the angle-resolved photoemission spectroscopy measurements over a wide range of material compositions.

(Some figures may appear in colour only in the online journal)

Contents

1. Introduction

Struggling for more than 20 years with a problem that it could not resolve despite tremendous efforts, the scientific community received in 2008 the announcement of the discovery of superconductivity at 26 K in an Fe-layered material [1] as a powerful electro-shock. The monopoly of copper oxides (cuprates) on high-T_c superconductivity was over. And yet, the future proved to be full of further surprises to those who started racing once more for the keys leading to higher T_cs.

Less than 4 years later, an impressive amount of data has been collected on these materials, accompanied by significant progress in our understanding of their exotic properties. Nevertheless, a consensus has not been reached on most aspects and it becomes very important to organize the pieces of the puzzle to get a more effective overall view. Up to now, there has been several review papers dealing with experiments on Fe-based superconductivity [2–7]. In this paper, we do not intend to repeat the content of previous reviews, but rather to provide a different perspective based on a particular experimental technique, namely angle-resolved photoemission spectroscopy (ARPES). ARPES is a powerful tool to access *directly* the momentum-resolved electronic structure of crystals, and thus it occupies a unique position when trying to understand their electronic behavior. In this review, we will cover some important aspects of Fe-based superconductors that have been addressed by ARPES, with a special emphasis on the superconducting (SC) gap.

This review is organized as follows. We first provide basic knowledge to understand simply what ARPES is and what are its advantages and limitations. In section 3, we describe the electronic structure of Fe-based superconductors, from core levels to the electronic states lying close to the Fermi level (E_F). The SC gap and its relationship to the electronic band structure will be discussed in section 4. We describe two models commonly used to explain superconductivity in these materials: the quasi-nesting model, which dominated the scene until only recently, and the local antiferromagnetic exchange pairing model, which now after the discovery of high-T_c superconductivity in the 122-chalcogenides many consider a better candidate to unify the SC pairing mechanism in Fe-based superconductors. Finally, before concluding this review, we will discuss the ARPES results in a broader context, where we compare ARPES with transport measurements.

2. Angle-resolved photoemission spectroscopy

2.1. Basic principles

The idea of photoemission spectroscopy, which is simply based on the conservation of energy, is to extract information on the electronic structure of crystals by measuring the kinetic energy of electrons ejected from the surface of a sample due to the interaction with a photon flux of known energy $h\nu$ and vector potential $\boldsymbol{A}$. ARPES is a sophisticated method among a variety of photoemission spectroscopies. In addition to the conservation of energy, ARPES takes advantage of the conservation of the in-plane momentum. Hence, the direction of emission of the photo-excited electrons is recorded as well as their energy. This procedure, illustrated in figure 1, allows the determination of the electronic band dispersions. Although ARPES measurements require much more time than angle-integrated photoemission spectroscopy (PES), which provides information on the electronic density of states (DOS) only, they give access to a more comprehensive determination of the electric band structure. More specifically, the ARPES signal $I(\boldsymbol{k}, E, \boldsymbol{A}, h\nu)$ is proportional to the one-particle spectral weight $A(\boldsymbol{k}, E)$, which is the probability of having an electron

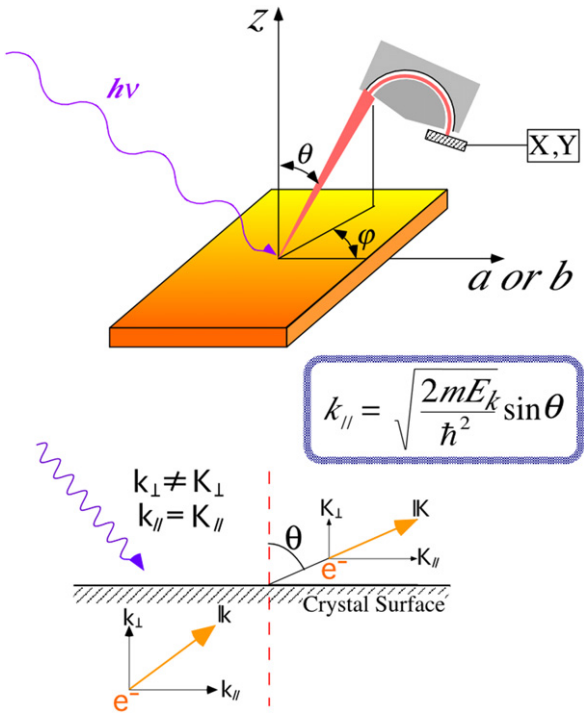

Figure 1. Schematic diagram explaining ARPES measurements. Under a flux of photons of energy $h\nu$, electrons are ejected from the surface of a sample (orange slab) at an angle (θ, φ) from the normal direction and detected with a high-resolution analyzer (in grey). The process implies the conservation of energy and in-plane momentum $(\boldsymbol{k}_{||})$.

in the sample with momentum $\boldsymbol{k}$ and energy E, times the Fermi–Dirac distribution $f(E,T)$:

$$I(\boldsymbol{k}, E, \boldsymbol{A}, h\nu) = M(\boldsymbol{k}, E, \boldsymbol{A}, h\nu)A(\boldsymbol{k}, E)f(E, T) \quad (1)$$

where M represents the photoemission matrix element determined by the photoemission process itself and carries no direct information on the band dispersion. However, M contains precious information on the nature of the electronic states probed.

The ARPES experimental data can be represented by colour images, where the colour scale gives the photoemission intensity, which is generally displayed as a function of energy and momentum. The energy is usually referenced to the leading edge of a metallic film spectrum, typically of gold, in electric contact with the sample. Although colour images give a more intuitive and natural representation of the electronic dispersion, they fail to reveal the precise spectral lineshape. For this reason, it is also convenient to represent the ARPES data with a series of curves of photoemission intensity as a function of energy at a fixed momentum k, or energy distribution curves (EDCs). Alternatively, one can display a series of curves of photoemission intensity as a function of momentum at a fixed energy E, or momentum distribution curves (MDCs).

2.2. Main advantages and limitations

As with any experimental techniques, ARPES has advantages and limitations. Its main advantage is quite obvious: it allows a *direct* determination of the electronic structure of

materials, including the Fermi surface and the band dispersion in the momentum space. This is crucially important when studying multi-band systems like Fe-based superconductors. The experimental information is irreplaceable since it is not obtained from a fitting procedure of several parameters on various models, which may turn out to be inadequate. Moreover, ARPES is suitable for relatively 'dirty' systems such as copper oxides or Fe-based superconductors, where doping is introduced through partial chemical substitution or the incorporation of interstitial dopants and vacancies. Such a doping process induces disorder, making determination of Fermi surfaces from quantum oscillation measurements difficult or even impossible under a low magnetic field. In contrast to transport techniques, ARPES is not limited to the Fermi surface, and it is sensitive to states away from the Fermi level, which is very useful when the physical properties are partly determined by high-energy states. Moreover, ARPES can be used to determine the orbital characters of the electronic states by taking advantage of selection rules involved in the photoemission process.

The main disadvantage of ARPES, which can also be regarded as an advantage when dealing with surface phenomena as in the topological insulators, is its surface sensitivity. To avoid surface contamination, single crystals of complex compounds are usually cleaved *in situ* and measured in a vacuum better than 10^{-9} Torr, the finite lifetime of the samples increasing as the vacuum improves. Hence, the lifetime of the samples can vary from a few hours to a few days. To maximize the sample lifetime, a vacuum in the 10^{-11} Torr range is routinely achieved using modern ultra-high vacuum systems such as in the Institute of Physics of the Chinese Academy of Sciences or in Tohoku University. Strictly speaking, ARPES measures the surface of materials, not the bulk. Nevertheless, the surface is *always* to some extent related to the bulk of materials. In other words, surface = bulk + δ. The reliability of the ARPES measurements when interpreting the physical properties of the bulk is thus determined by the size of δ, which is compound-dependent. There are several ways to check if δ is qualitatively small or large. δ can be considered small under the following conditions:

(i) Low-energy electron diffraction (LEED) pictures do not show obvious surface reconstruction.
(ii) The surface carrier doping, as determined from the Luttinger theorem, is consistent with that of the bulk.
(iii) The Fermi surface evolves smoothly with doping.
(iv) The electronic structure (band dispersion, gap size, etc) varies with k_z, in sharp contrast to pure surface states.
(v) The SC gap observed by ARPES closes at the bulk T_c.
(vi) The core levels of the relevant elements are not doubled.
(vii) The band dispersions are similar, albeit for some renormalization, to local density approximation (LDA) predictions.
(viii) No unexpected band folding is observed by ARPES.
(ix) Gaps measured by ARPES are consistent with gaps measured from bulk-sensitive probes. It should be noted that ARPES bulk sensitivity is highly enhanced by the use of very low photon energies ($h\nu < 9$ eV) [8, 9] or high photon energies ($h\nu > 500$ eV) [10].

Fortunately, several Fe-based superconductors fulfil these requirements. Although the influence of the surface cannot be predicted systematically, the crystal structure symmetry of layered systems guides us to determine which compound is susceptible to present a surface problem. When the cleaving plane is unique and occurs between two symmetric layers, the two cleaved pieces are perfectly symmetric. The surface is thus usually non-polar and surface effects are expected to be minimal. For example, that case corresponds to the 11 and 111 structural phases of Fe-based superconductors. On the other hand, when the structure presents more than one equivalent cleaving plane leading to more than one possible surface exposed, the surface may be highly polar. The surface doping in this case is not representative of the bulk. $YBa_2Cu_3O_{7-\delta}$ is one of the most famous structures belonging to this category, in which the 1111-pnictide structure falls as well. Nevertheless, ARPES can be used in this case to get a reasonable idea of the band structure, exact doping and k_z dispersion put aside. Another important situation is the one when cleaving occurs exactly at a symmetry plane occupied by one layer of atoms. To account for electrostatic stability, only half of the atoms remain on the cleaved surface. The surface may reconstruct or not. The experiment alone and the use of the criteria described above can determine whether the experimental results are representative of the bulk for the electronic states of interest. Special attention should be given to the 122 family of Fe-pnictides, which belongs to this category. Surface effects have been reported in $SrFe_2As_2$ [11]. Interestingly, such an effect is not observed in hole-doped $Ba_{1-x}K_xFe_2As_2$, which satisfies the criteria enumerated above, in agreement with an LEED and scanning tunnelling microscopy (STM) study reporting the absence of surface reconstruction in $BaFe_2As_2$ [12]. Furthermore, as shown below, the 122-pnictides share similar electronic structures and SC gap functions with other Fe-based superconductors with ideal cleaving planes, suggesting that even supposing that a small distortion occurs in the (Ba, K) layer at the cleaved surface, the effect on the Fe electronic states are negligible.

2.3. Brillouin zone notation

Unfortunately, the notation used in ARPES studies of Fe-based superconductors to describe high-symmetry points in the momentum space is not homogeneous, and two main representations are usually found in the literature. In the first one, only the Fe atoms are considered. The Fe atoms form a square lattice of parameter a, which corresponds to a square Brillouin zone (BZ) of size $2\pi/a$. In this *1 Fe/unit cell* or *unreconstructed* description, the zone centre Γ and the M point correspond to $(0, 0)$ and $(\pi/a, 0)$, respectively, while the X point is defined as $(\pi/2a, \pi/2a)$. The Γ–M direction is associated with momentum along the Fe–Fe bounding. Alternatively, one can prefer to consider the 'real' BZ and take into account the effect of the alternative distribution of chalcogen and pnictogen atoms up and down the Fe plane. The unit cell parameter becomes $a' = a\sqrt{2}$. In this *2 Fe/unit cell* or *reconstructed* description, M = $(\pi/a', \pi/a')$ and $X = (\pi/a', 0)$. To add to the confusion, some authors

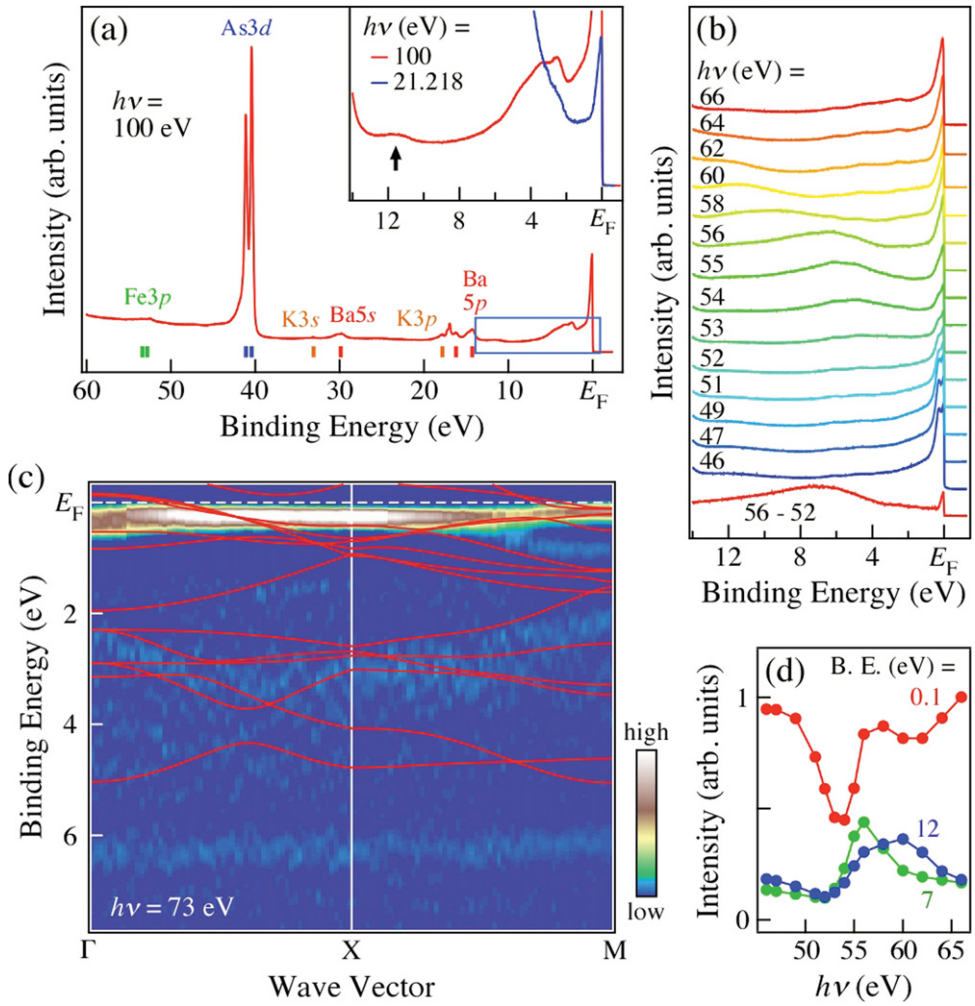

Figure 2. (*a*) Wide range EDC near Γ showing shallow core levels marked by vertical bars above the *x*-axis. The inset magnifies the valence band (VB) and a possible satellite peak at ∼12 eV, and highlights the difference between spectra taken at 100 and 21.2 eV. (*b*) VB near Γ measured at different photon energies (46–66 eV). All EDCs are normalized by the photon flux. (*c*) Intensity plot of second derivatives of spectra along Γ–X and X–M. LDA bands (red lines) are plotted for comparison. (*d*) Photon energy dependence of the EDC intensity shown in (*b*) obtained at binding energies 0.1, 7 and 12 eV. Reprinted with permission from [13].

rather define $M = (\pi/a', 0)$ and $X = (\pi/a', \pi/a')$. Unless specifically indicated, we use the 1 Fe/unit cell representation by default in this review.

3. Electronic structure

The electronic properties of a material are governed by its own electronic structure, which is determined by the composition and the arrangement of the atoms from which it is made. All Fe-based superconductors are characterized by the presence of Fe layers. It is thus quite natural that they share similar electronic structure. Since it has been studied in more detail, we begin this chapter by presenting ARPES results on optimally doped $Ba_{0.6}K_{0.4}Fe_2As_2$ as a typical Fe-based superconductor. We will then review ARPES results obtained on several other Fe-based materials.

3.1. Optimally doped $Ba_{0.6}K_{0.4}Fe_2As_2$

The core level spectrum displayed in figure 2(*a*) is consistent with the chemical composition of $Ba_{0.6}K_{0.4}Fe_2As_2$. From high to low binding energies, we can distinguish unambiguously core levels associated with Fe3p (52.4, 53.0 eV), As3d (40.4, 41.1 eV), K3s (33.0 eV), Ba5s (29.7 eV), K3p (17.8 eV) and Ba5p (14.2, 16.2 eV) [13]. We also observe a weak peak around 12 eV, whose origin remains unclear. Although it could come from As4s states, we note that several divalent Fe compounds, such as FeO, exhibit a peak at a similar energy attributed to a satellite state of the $Fe3d^5$ configuration [14]. The strongest core level peaks are those corresponding to the $As3d_{5/2}$ and $As3d_{3/2}$ levels. Although As atoms are located just below the cleaved surface, it is worth mentioning that unlike GaAs, for which a set of surface components are observed 0.4 eV below the peak energies, the As3d levels in $Ba_{0.6}K_{0.4}Fe_2As_2$ do not show an obvious additional component that could result from a surface reconstruction. It is thus reasonable to assume that the electronic states of Fe atoms, which are located below the first As layer, are not significantly affected by the surface termination.

The nature of the electronic states within about 8 eV below E_F can be determined by investigating their photon energy dependence. The inset of figure 2(*a*) compares the spectra of

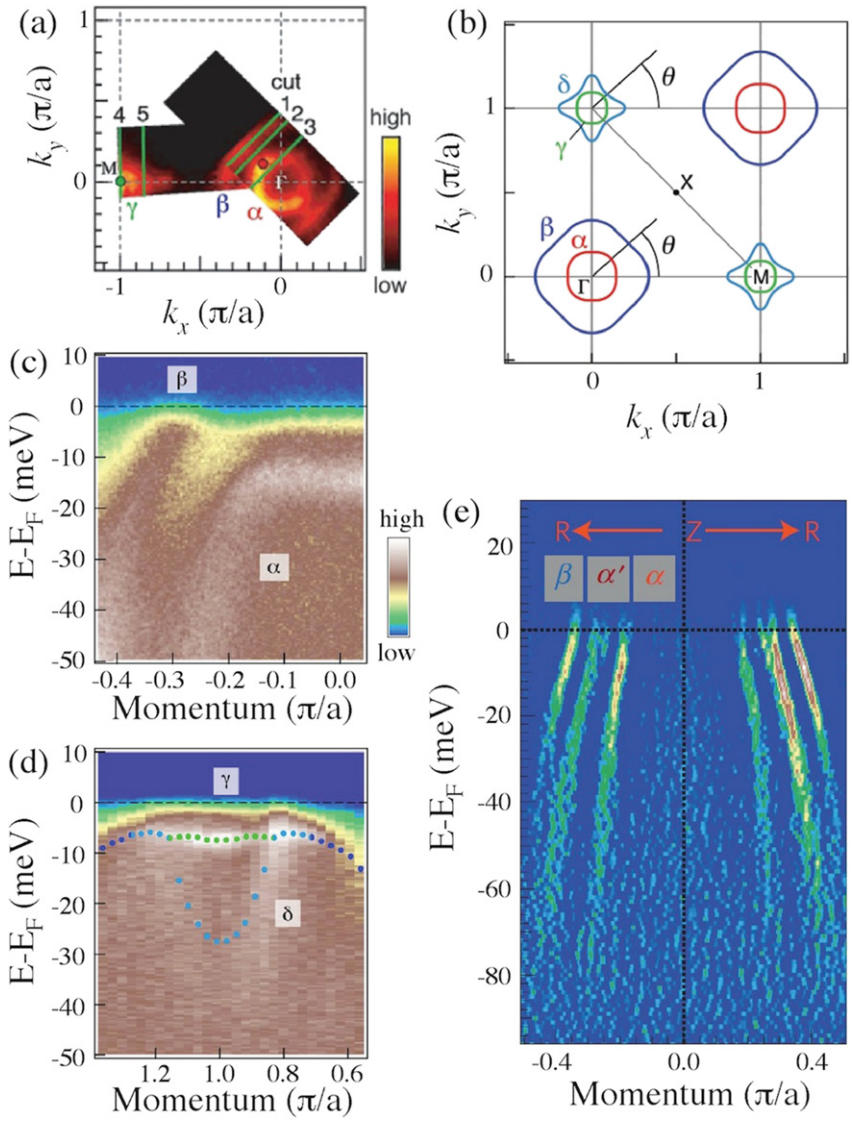

Figure 3. (*a*) FS contour determined by plotting the ARPES spectral intensity integrated within ±10 meV with respect to E_F. (*b*) Schematic view of the four FS sheets with a definition of the FS angle (θ). (*c*) Intensity plot near Γ measured at $T = 15$ K. (*d*) Intensity plot near M measured at 15 K. Dots are EDC peak positions. (*e*) Second derivative plot of the dispersion along Z–R ($k_z\pi$) measured using 32 eV photons. Three hole-like bands (α (inner), α' (middle) and β (outer)) are observed. (*a*) Reproduced with permission from [17], copyright 2008 by the European Physical Society. (*b*) Reproduced with permission from [18], copyright 2009 by the European Physical Society. (*c*), (*d*) Reproduced with permission from [13]. (*e*) Reprinted by permission from Macmillan Publishers Ltd: *Nature Phys.* [19], copyright 2011.

$Ba_{0.6}K_{0.4}Fe_2As_2$ at 21.2 and 100 eV. While the former photon energy is more sensitive to As4s states, the latter enhances Fe3d states. We thus conclude that the sharp peak within 1 eV below E_F originates mainly from Fe3d states and the states at higher biding energy mainly from As4s orbitals, in agreement with LDA band calculations [15]. This assessment is reinforced by the detailed photon energy evolution of the low-energy states across the Fe3p → Fe3d resonance at 56 eV, which is illustrated in figure 2(*b*). The difference of the spectra recorded at 56 eV (at the resonance) and at 52 eV (below the resonance) exhibits two features: a sharp peak near E_F and a broad peak centred around 7 eV, which can be regarded as the coherent and incoherent parts of the Fe3d states, respectively. While the photoemission intensity near E_F shows an anti-resonance profile, the incoherent part at 7 eV has a Fano-like resonance profile (see figure 2(*d*)), which is similar to the Fe3d states in FeO [14].

The Fe3d and As4s levels within 8 eV below E_F are dispersive, as illustrated in figure 2(*c*) by the intensity plot of second derivative, for the Γ–M and Γ–X high-symmetry lines. When renormalized by a factor 2, LDA band calculations [16] at this doping capture some overall features observed experimentally. This indicates that correlations in this material are not negligible. Interestingly, band renormalization seems more important at a lower binding energy, as discussed below.

We now turn our attention to the states closer to the Fermi energy, which mainly govern the electronic properties of materials. The Fermi surface (FS) of $Ba_{0.6}K_{0.4}Fe_2As_2$ recorded with the He Iα resonance line is displayed in figure 3(*a*) [17], and a schematic version is given in

figure 3(*b*). It illustrates the multi-band nature of the Fe-based superconductors. ARPES intensity plots along cuts passing through or close to the Γ point allow us to identify at least two hole-like bands crossing E_F. Hereafter, we call α and β the bands giving rise to the small and large Γ-centred FS pockets, respectively. These band are quite clear in the intensity plot given in figure 3(*c*) (below T_c). Similarly, the ARPES intensity plots along cuts passing near the M point reveal two distinct electron-like FS pockets, γ and δ, as shown in figure 3(*d*). Their origin can be understood from the hybridization of ellipses elongated towards the Γ–M direction and folded across the Γ–X plane due to the BZ reconstruction induced by the alternative positions of As atoms below and above the Fe layer.

Although very high energy resolution can be achieved in ARPES measurements performed with a He discharging lamp, the results are confined to a single k_z value. Using the tunability of synchrotron radiation, ARPES experiments can reveal a small warping in the band dispersion along k_z [19, 20]. More importantly, an additional hole-like band, which is almost degenerate with the α band at the zone centre, is resolved as k_z increases towards $Z = (0, 0, \pi/c)$ (where $c = 6.5$ Å is the lattice parameter of the primitive unit cell and the distance between two Fe layers), as illustrated in figure 3(*e*). The synchrotron data indicate that He ια radiation corresponds approximately to $k_z = 0$, explaining why this third band was not observed in the earliest ARPES experiments. The results obtained at different values of k_z have several significant consequences. (i) They are consistent with LDA band calculations, which all predict three Γ-centred hole-like bands and two M-centred electron-like bands. (ii) They also confirm that the surface of $Ba_{0.6}K_{0.4}Fe_2As_2$ does not carry extra charge, unlike $YBa_2Cu_3O_{7-\delta}$. Indeed, assuming a double degeneracy for the α band, one can show that the algebraic FS area satisfies the Luttinger theorem with the bulk doping [17, 18]. (iii) Finally, the k_z warping of the electronic structure proves that the electronic states measured by ARPES *cannot* be pure surface states and that ARPES captures at least the essence of the bulk electronic properties.

It is interesting to note that the Fermi velocities determined from ARPES differ from the values predicted by LDA calculations by a factor greater than the renormalized factor of 2 obtained for the overall band structure, indicating that low-energy states are further renormalized [13]. Interestingly, such an observation has also been made for other strongly correlated electron systems such as the cuprates [21] and cobaltates [22]. For practical purposes, the band structure can be parametrized using a tight-binding-like model (table 1) [13]:

$$E^{\alpha,\beta}(k_x, k_y) = E_0^{\alpha,\beta} + t_1^{\alpha,\beta}(\cos k_x + \cos k_y) + t_2^{\alpha,\beta} \cos k_x \cos k_y \quad (2)$$

and

$$E^{\gamma,\delta}(k_x, k_y) = E_0^{\gamma,\delta} + t_1^{\gamma,\delta}(\cos k_x + \cos k_y) + t_2^{\gamma,\delta} \cos k_x/2 \cos k_y/2. \quad (3)$$

Since ARPES can reveal the unoccupied part of the band structure for only a few k_BT's, mild constraints must be used for the fit. The results obtained with this model allow an estimation of the effective masses and reveal a total renormalization factor of about 3–4 for the near-E_F bands, in addition to providing essential parameters to calculate some thermodynamical parameters such as the Sommerfeld coefficient [13].

Table 1. Tight-binding fit parameters; from [13].

	α	β	γ	δ
E_0	−0.24	−0.025	0.7	0.7
t_1	0.16	0.013	0.38	0.38
t_2	−0.052	0.042	0.8	−0.8

3.2. *Magnetic parent compounds*

The parent compounds of both cuprates and Fe-based superconductors have magnetically ordered states, with superconductivity emerging away from the magnetic ordered phase. The study of these materials is therefore of prior interest. Unlike the cuprates though, the parent compounds of the Fe-based superconductors are generally metallic, which is an important advantage for ARPES studies. Hence, ARPES investigations have been reported on the parent compounds of the 122-pnictide [11, 23–34], 11-chalcogenide [35, 36] and 111-pnictide [37] systems.

Magnetic ordering in the parent compounds is accompanied by a reduction of the BZ and subsequent band folding. The relationship between the unreconstructed, reconstructed and 2D magnetic BZ in the 122 phase is described in figure 4(*a*), which also shows the FS of $BaFe_2As_2$ well below the spin-density wave (SDW) transition $T_{SDW} = 138$ K. The intensity mapping indicates FSs of equivalent sizes around the Γ and M points. The FS contours are better represented by the second derivative of the intensity map shown in figure 4(*b*), which reveals almost identical patterns around Γ and M, confirming band folding across the magnetic BZ boundaries. However, these patterns are quite unusual. In particular, strong photoemission intensity spots are observed near $\Lambda = (0, 0.75)$ and equivalent symmetry points, away from high-symmetry points [25]. As temperature increases, these high-intensity spots remain quite clear below T_{SDW}. Above that critical temperature, the spots are hard to identify, suggesting that they originate from the magnetic state.

Interestingly, the intensity spots at the Λ point cannot emerge from a single band. A careful analysis shows that two bands cross the Fermi level around the Λ point. Even more surprising is the almost conical band structure at that particular momentum point, which cannot be produced by simple band folding. Using the broadening of the Fermi cutoff at higher temperature, one can access states above E_F within a range of a few k_BTs. The spectra recorded at 100 K, which has been divided by the Fermi function convoluted by the energy resolution function, is displayed in figure 5(*a*). Along with its second derivative intensity plot (figure 5(*b*)), it reveals an X-like pattern rather than a simple Λ-like one. This strongly suggests the presence of a Dirac cone [25], which is further confirmed by the absence of a hybridization gap at the cone apex, as illustrated by the EDCs in figure 5(*c*).

As shown in figure 5(*d*), the analysis of the low-temperature band structure of $BaFe_2As_2$ suggests that the

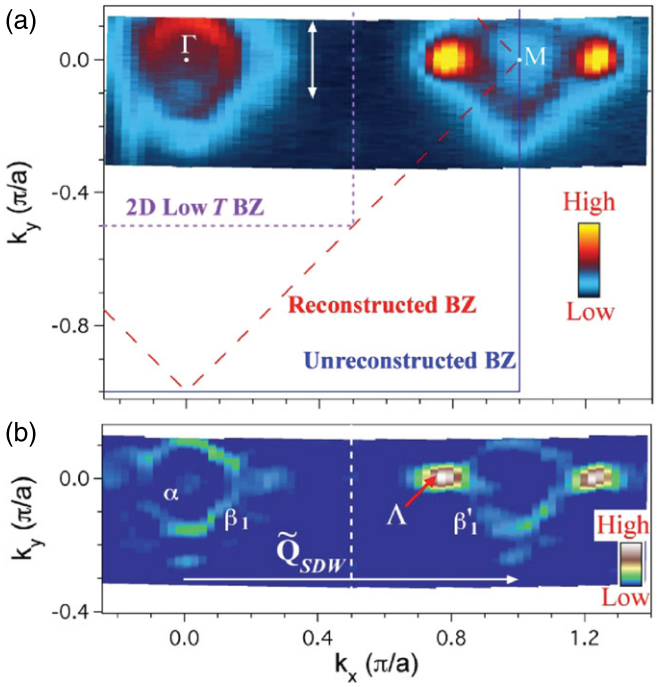

Figure 4. (*a*) FS mapping (25 K) obtained by integrating the photoemission intensity in a 20 meV window centred at E_F. The FS is described in terms of the unreconstructed BZ. The double arrow indicates light polarization. (*b*) Corresponding second derivative intensity plot. $\tilde{Q}_{SDW}$ is the in-plane projection of the SDW wave vector. Reprinted with permission from [25], copyright 2010 by the American Physical Society.

Fermi velocity v_F varies slightly around the Dirac cone, from 290 to 360 meV Å, with an average of 330 ± 60 meV Å, which is compatible with the symmetry of the Λ point [25]. The apex is found at 1 ± 5 meV above E_F, implying a very small hole FS pocket covering only around 10^{-3}% of the first BZ, as suggested by figure 5(*e*). Interestingly, bulk-sensitive quantum oscillation measurements led to similar results for the Fermi velocity [38], as well as for the presence of small FS pockets [39, 40].

The access to v_F around the Dirac cone allows a 3D reconstruction of the Dirac cone, which is given in figure 6(*a*). Although such Dirac cones in the magnetic phase of these materials were not commonly expected, they were predicted by Ran *et al* [41], who argued that even in the presence of perfect nesting, the degeneracy of the band structure at the Γ and M points must lead to nodes in the SDW gap function. Indeed, their calculations indicate the formation of Dirac cones at the SDW gap nodes. The SDW gap increases away from the Dirac cone, in agreement with ARPES measurements of the leading edge shift around the M point (as defined in figure 6(*b*)), which are shown in figure 6(*c*). Figures 6(*d*) and (*e*) confirm that the electronic states are gapped away from the Dirac cone. Interestingly, ARPES measurements indicate that the electron-like bands have gaps of ∼30 and ∼50 meV. In a first approximation, considering that the Dirac cone apex is almost at the Fermi level, the corresponding full SDW gaps can be estimated at ∼60 and ∼100 meV, which is not far from the values of 45 and 110 meV determined from optical data [42]. The presence of Dirac cones in the Fe-based superconductors goes much beyond superconductivity and connects several materials which appear completely different at the first sight [43]. For example, time-reversal symmetry and C_3 crystal structure induce Dirac cones in graphene, a single layer of carbon atoms on a triangular lattice. Dirac fermions also emerge at the surface of the newly discovered topological insulators as a consequence of spin–orbit coupling. Finally, cuprates, which have a Mott insulating parent compound, display a Dirac cone at the nodal point of their d-wave SC gap once they are doped with impurities. The massless dispersion common to all these materials is believed to play a major role in the next generation of electronic and spintronic devices. Not only Fe-based superconductors now join this category of materials, but they also constitute the first illustration by ARPES of an anisotropic Dirac cone dispersion. In addition, this discovery shows the importance that orbital characteristics may play in Fe-based superconductivity [43].

Recent density mean-field theory (DMFT) calculations in the magnetic state of $BaFe_2As_2$ show a very nice consistency with experimental data [44]. Unlike most ARPES experiments performed on twinned samples, the calculations exhibit the expected two-fold symmetry rather than a four-fold symmetry. To reveal the in-plane anisotropy of the band structure from ARPES, samples have to be untwined *in situ* before the experiment [33, 34].

Contrary to optimally doped $Ba_{0.6}K_{0.4}Fe_2As_2$, where only a small warping of the band structure is reported [19], a strong variation of the electronic band structure along the k_z direction is found experimentally [23, 24, 26–28, 31–33]. However, only the α band shows a significant k_z-dependence, with a periodicity of $4\pi/c$ due to the periodicity of the primitive unit cell. While a 3D α pocket centred at Γ has been reported for $CaFe_2As_2$ [24], some reports on $BaFe_2As_2$ suggest that the α band crosses E_F at every k_z [27]. In contrast to the α band, the bands forming the Dirac cone, as well as the electron-like bands at the M point, are only weakly sensitive to k_z. Interestingly, one report on $CaFe_2As_2$ clearly associates the k_z variations to the SDW state [24]. Above T_{SDW}, the band structure does not show obvious modulations along k_z.

The 11-chalcogenide system has the simplest structure of all Fe-based superconductors. Interestingly, its magnetic ground state is also different. Unlike $BaFe_2As_2$, the antiferromagnetic wave vector of FeTe points in the Γ–X direction. Consequently, the electronic band structure folds with respect to different magnetic zone boundaries below the ordering temperature. This effect has been observed directly by ARPES [35, 36], where bands are folded to the X point, as expected.

3.3. Doping evolution of the electronic states in the 122-pnictide system

The 122-pnictides have been the most studied among the Fe-based superconductors and we already have a rough overview of the phase diagram as seen by ARPES. The schematic phase diagram of these materials is illustrated in figure 7(*a*). Both the electron-doped and the hole-doped sides show superconductivity and antiferromagnetism. A complication occurs in the electron-doped side, where the

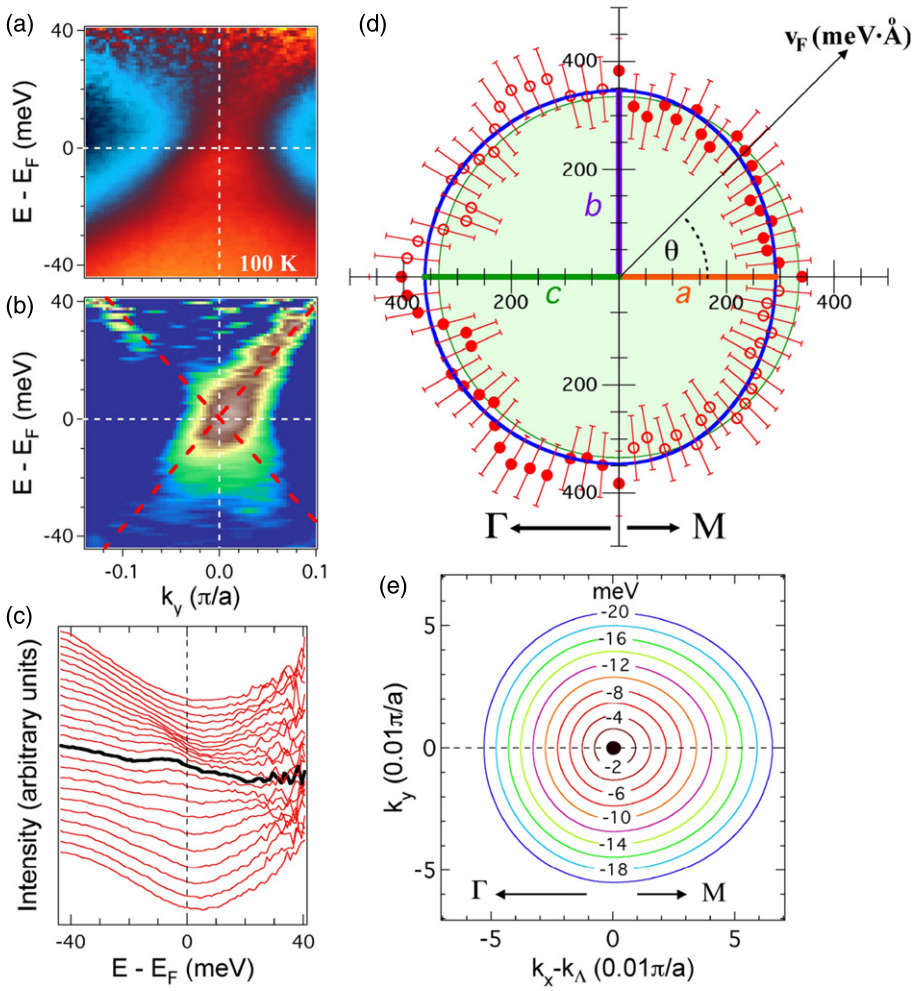

Figure 5. (*a*) ARPES intensity spectra of $BaFe_2As_2$ at the Λ point ($\theta \sim 90^\circ$) recorded at 100 K, after division by the Fermi–Dirac function convoluted with the instrumental resolution function. (*b*) Corresponding second derivative intensity plot. Long dashed lines are drawn as a guide for the eye. The corresponding EDCs are given in (*c*), where the bold EDC refers to the Λ point. (*d*) Polar representation of v_F around the Λ point (25 K). Open and closed circles represent data measured and data obtained by reflection with respect to the Γ–M symmetry line, respectively. The large filled circle represents the average value of v_F while the thick line is a fit of the data to the two-ellipse model described in the text, with parameters *a*, *b* and *c*. (*e*) Contour plot of the electronic dispersion below E_F around the Λ point, as calculated from our model. The small filled circle represents the FS associated with the cone. Reprinted with permission from [25], copyright 2010 by the American Physical Society.

SDW transition does not coincide with the structural transition that accompanies the SDW transition in the hole-doped case. However, the main difference between the two sides of the phase diagram is the respective sizes of the antiferromagnetic and SC regions. The SC critical temperature reaches a maximum of about 37 K in the hole-doped case, which is obtained at a doping of about 0.2 doping hole per Fe, whereas it tops only around 25 K in the electron-doped materials, with an optimal doping that is roughly 0.08 electron dopant per Fe. Moreover, the SC dome is wide for hole doping and a SC tail survives up to the end of the phase diagram with KFe_2As_2. It is likely that the reason for such behavior lies in the electronic band structure itself.

With the electronic carrier concentration varying, the FS of bulk states must evolve according to the Luttinger theorem, with the size of electron-like FS pockets increasing (decreasing) as we add electrons (holes), and the size of hole-like FS pockets behaving exactly the other way. An illustration of the size evolution of the FS pockets in hole-doped $Ba_{1-x}K_xFe_2As_2$ around optimal doping is given in figures 7(*c*)–(*e*). For convenience, the M-centred electron-like FS pockets have been shifted to the Γ point. As expected, the size of the α and β hole-like FS pockets increases with the hole carrier concentration increasing from underdoped $Ba_{0.75}K_{0.25}Fe_2As_2$ [49] to overdoped $Ba_{0.3}K_{0.7}Fe_2As_2$ [48] while the size of the electron-like pockets is reduced. Precise analysis of the algebraic FS area is consistent with the bulk concentration in each case.

To characterize the similarity between the size of the α FS and that of the M-centred electron-like FS pockets, here we extend the notion of nesting beyond its strict meaning. In 2D, if two circular electron-like and hole-like pockets overlap completely under translation by the momentum $\boldsymbol{Q}$, the bare static spin susceptibility $\chi_0(\boldsymbol{q}, E = 0)$ diverges logarithmically as $\boldsymbol{q}$ approaches $\boldsymbol{Q}$. This singularity defines perfect nesting with the important consequence that the random phase approximation (RPA) susceptibility diverges as well, i.e. the system becomes unstable toward an SDW with

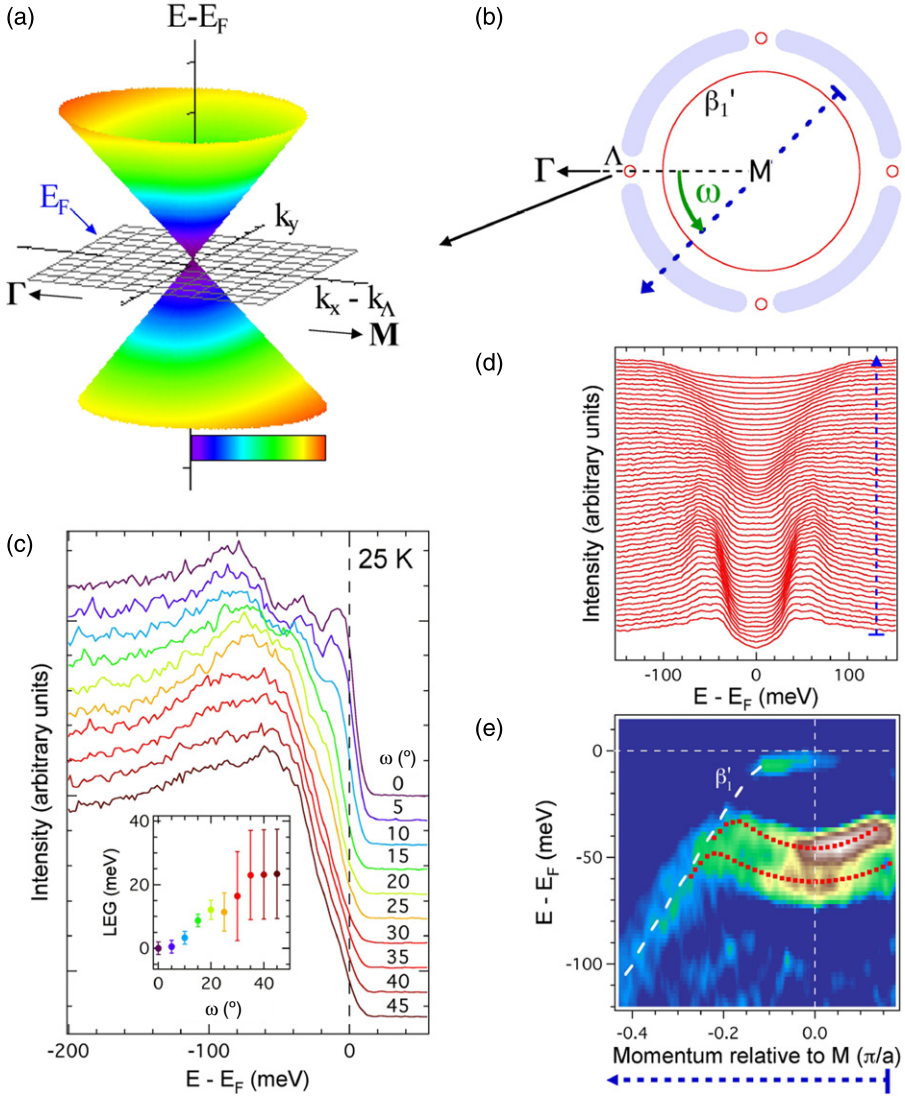

Figure 6. (*a*) 3D representation of the Dirac cone at Λ. The colour scale indicates the distance from Λ. (*b*) Schematic FS around the M point. The folded α band, which is barely touching E_F, is not indicated. Shaded areas indicate gapped regions and the dashed arrow indicates the orientation of the ARPES cut associated with (*d*) and (*e*). (*c*) Minimum gap location of EDCs (25 K) as a function of the angle ω defined in (*b*). The inset shows the leading edge gap (LEG) as a function of ω after a 3.5 meV shift (see the text). (*d*) Symmetrized EDCs (25 K) along the cut indicated in (*b*). (*e*) Second derivative intensity plot (25 K) along the cut indicated in (*b*). The vertical dashed line indicates the M point. Reprinted with permission from [25], copyright 2010 by the American Physical Society.

wave vector $\boldsymbol{Q}$ for arbitrarily weak interactions. Although $\chi_0(\boldsymbol{q}, E = 0)$ no longer diverges at $\boldsymbol{Q}$ if the size and shape of the FSs start to deviate slightly from each other, the susceptibility can remain peaked at $\boldsymbol{Q}$, and thus moderate interactions can still drive the system into an SDW or charge-density wave (CDW) transition in the presence of fluctuations near the wave vector $\boldsymbol{Q}$. The precise behavior of the susceptibility for what becomes natural to call *near-nesting* or *quasi-nesting* can be analytically understood in terms of a cutoff for the divergence arising from the deviation to perfect nesting [50]. Since the FSs are simply the constant energy contours of the energy dispersions at zero energy, the electron-like and hole-like pockets can be even better nested by low-energy contours close to the Fermi level. This implies that quasi-nesting is even more robust for dynamical fluctuations, for which $\chi_0(\boldsymbol{q}, E)$ is very much enhanced, producing strong low-energy fluctuations with wave vector $\boldsymbol{Q}$, as indicated by the numerical renormalization group approach [51]. In practice, we will say that the hole-like and electron-like FSs are quasi-nested if for large portions of the hole-like FS, we can find a small wave vector $\delta \boldsymbol{q}_i$ and a small energy δE_i so that the Fermi wave vector $\boldsymbol{k}_{\mathrm{F},i}$ on the hole-like FS can be connected by the wave vector $\boldsymbol{Q} + \delta \boldsymbol{q}_i$ to one point on the δE_i energy contour of the electron-like dispersion.

Within the extended notion of nesting described above, the α FS is well quasi-nested with the M-centred electron-like FS pockets in the optimally doped system. Unavoidably, the quasi-nesting conditions must evolve while doping the system. With underdoping, the size of the β FS shrinks but is still far to match the FS at the M point. In the meantime, the quasi-nesting of the M-centred electron FSs and the α FS deteriorates only slightly, mainly along the Γ–M direction. In the slightly overdoped region, the quasi-nesting conditions are more severely affected. Yet each FS survives

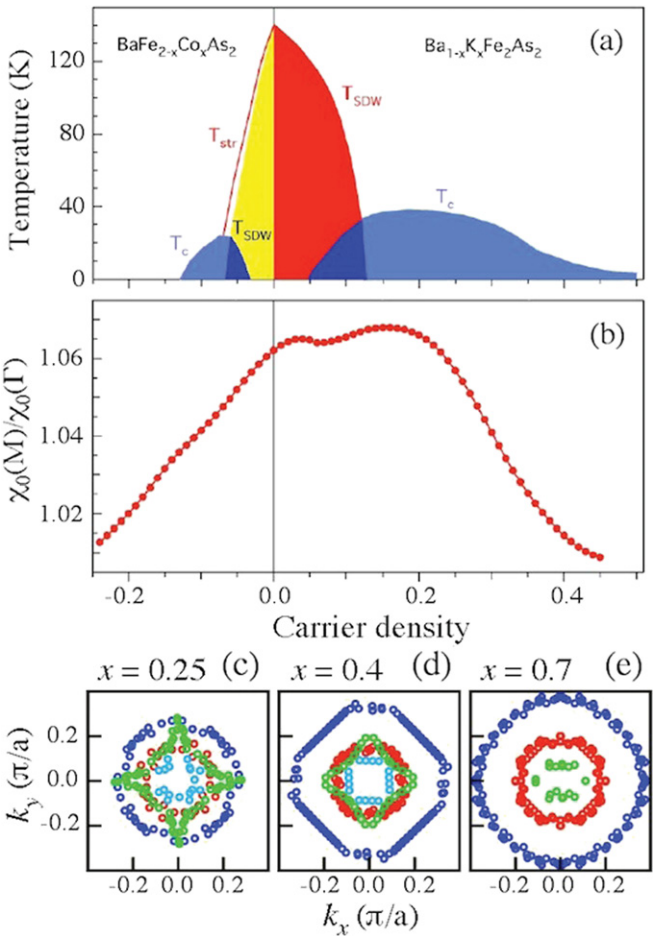

Figure 7. (*a*) Phase diagram of the hole- and electron-doped Ba-122 systems taken from [45] and [46], respectively. T_c, T_{SDW} and T_{str} refer to the SC, the SDW and the tetragonal to orthorhombic structural transitions, respectively. (*b*) Doping dependence of the Lindhard function χ_0 at the M point (quasi-nesting wave vector) normalized by its value at the zone centre. The Lindhard function was obtained using LDA calculations. (*c*)–(*e*) Experimentally determined k_F points of the α, β and γ/δ bands (red (grey), blue (dark grey), and green (light grey) circles, respectively). The k_F points of the γ/δ FSs are shifted by $\boldsymbol{Q} = (-\pi, 0)$. (*a*), (*b*) Reprinted with permission from [47], copyright 2011 by the American Physical Society. (*c*)–(*e*) Reprinted with permission from [48], copyright 2011 by the American Physical Society.

and antiferromagnetic scattering between Γ and M is still expected. This statement is no longer true when doping the system even more with holes.

Sato *et al* reported a detailed analysis of the band structure of fully K-substituted $Ba_{1-x}K_xFe_2As_2$ [52]. The main finding of this report is the total absence of electron-like FS at the M point in KFe_2As_2, which is equivalent to a suppression of the quasi-nesting condition between hole-like and electron-like FS pockets. Instead, four small FSs, elongated along the Γ–M direction, emerge away from M, as indicated in figure 8(*a*). Interestingly, this dramatic change in the FS topology is not caused by a reconstruction of the band structure, but simply by a ∼20 meV shift of the chemical potential as compared with the optimally doped compound (see figure 8(*b*)).

The optimally electron doped $BaFe_{1.85}Co_{0.15}As_2$ system ($T_c = 25.5$ K) was first studied by Terashima and co-workers [53]. Due to the chemical potential shift that accompanies electron doping, the α FS pocket is totally absent in this material. Instead, only the β FS survives around the Γ point. Nevertheless, its size is significantly reduced. On the other hand, the M-centred electron-like FS pockets expand, as expected, and the size of the inner electron-like pocket at M becomes similar to the size of the β pocket, suggesting that antiferromagnetic scattering can become important for this composition. As with its hole-like counterpart, this is not the case when the system is extremely electron-doped. Sekiba *et al* demonstrated the absence of hole-like FS pocket and thus the disappearance of quasi-nested FSs in $BaFe_{1.7}Co_{0.3}As_2$, in which T_c vanishes [54]. Indeed, even the β band sinks completely below E_F at that high electron doping. In contrast, the M-centred electron-like FSs become larger than in $BaFe_{1.85}Co_{0.15}As_2$, as required by the Luttinger theorem. We note that this change in the FS topology as compared with the optimally doped system is induced by a chemical potential shift of about 20 meV due to electron doping and that the overall band structure is preserved [54].

Unlike the hole-doped side of the phase diagram, traces of what can be attributed to long-range antiferromagnetism survive at quite high electron doping in the underdoped regime, at least when using normalized doping x/x_c. Indeed, the bright spots attributed to the band-folding-induced Dirac cone in the parent compound [25] are observed until the onset of superconductivity [55]. For the electron-doped compounds though, the bright spots evolve into small hole-like pockets [55]. We note that their elongated shape is consistent with the anisotropy of the Dirac cone [25].

A critical observation in the 122-pnictides is that, in addition to the band folding that is present in the antiferromagnetic regime, the band structure of these materials does not vary significantly with doping. Instead, the electronic states near the Fermi level are tuned by a simple shift of the chemical potential with doping. Neupane *et al* tracked the position of the bottom of the M-centred electron-like bands as a function of doping on both side of the phase diagram [47]. Similarly, the authors also estimated the shift in the position relative to E_F of the Γ-centred hole-like bands by matching their electronic dispersions, as illustrated in figure 8(*c*). Interestingly the shifts of the electronic band structure at the Γ and M points coincide, at least at the first order. More importantly, figure 8(*d*) shows that the chemical potential shift determined by this method is in good agreement with that estimated from LDA calculations after renormalization of the band width by a factor of 4 [47] to take into account the stronger renormalization observed for the electronic states very near E_F [13]. This conclusion has two important consequences. First, it confirms experimentally that the system is really doped through the substitution of Fe by Co, and that this substitution does not affect the effective masses of the system significantly, in contrast to speculations from a theoretical model that suggest that the Co substitution does not dope the system [56]. Second, it suggests that renormalized LDA band calculations can be used to predict various electronic behaviors of these compounds, at least at the first order and away from long-range antiferromagnetic ordering. Starting

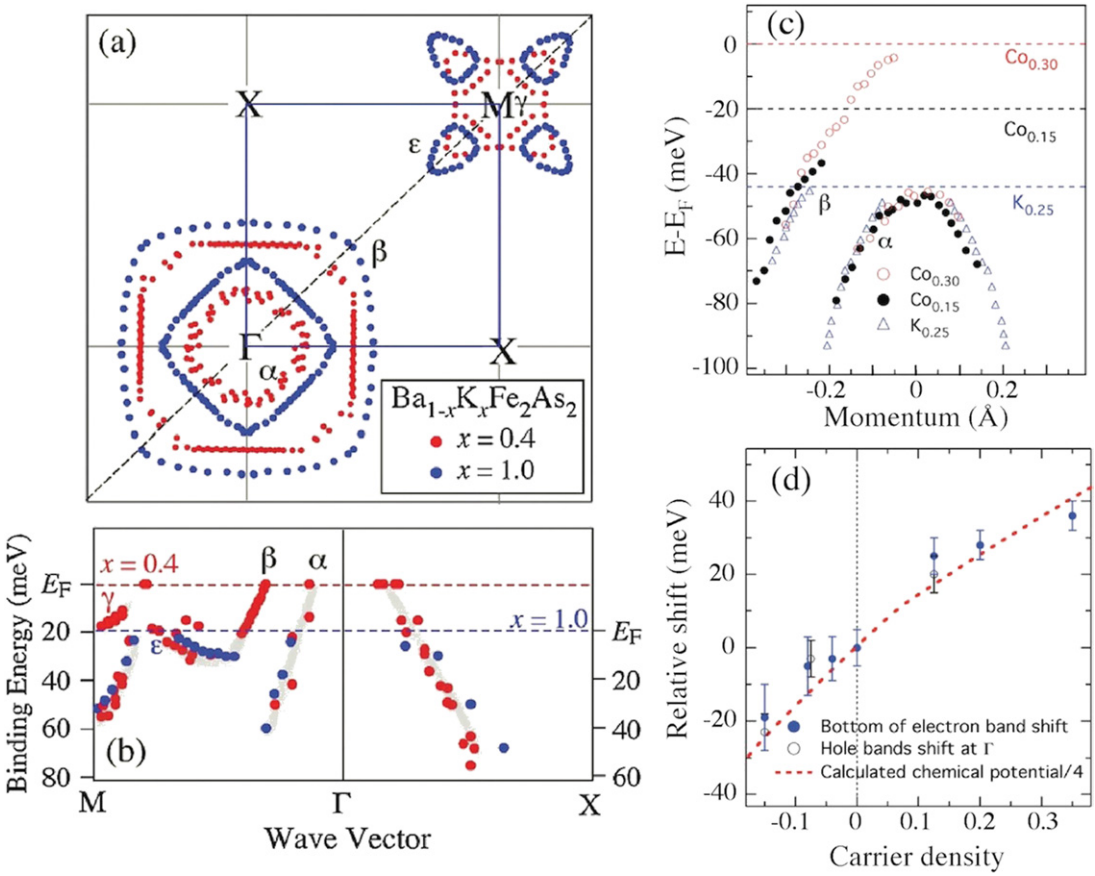

Figure 8. (*a*) Comparison (in the 2 Fe/unit cell notation) of experimentally determined k_F points between overdoped KFe_2As_2 ($T_c = 3$ K) and optimally doped $Ba_{0.6}K_{0.4}Fe_2As_2$ ($T_c = 37$ K) [17] (blue and red circles, respectively). The k_F points are symmetrized by assuming a four-fold symmetry with respect to the Γ and M points. (*b*) Experimental band dispersion in the vicinity of E_F for two high-symmetry lines determined by tracing the peak position of the ARPES spectra. The chemical potential of the KFe_2As_2 sample is shifted downward with respect to that of the $Ba_{0.6}K_{0.4}Fe_2As_2$ sample. (*c*) Fits of the α and β bands for cuts passing through the Γ point. The bands have been shifted to match the band slopes. (*d*) The blue dots are the VB shifts shown in (*c*) and the red dash curve is the LDA calculated values of the chemical potential divided by a factor of 4. The black dots correspond to the relative shifts derived from (*c*), with the shift of the $BaFe_{1.7}Co_{0.3}As_2$ compound fixed arbitrarily on the renormalized LDA curve. (*a*), (*b*) Reprinted with permission from [52], copyright 2009 by the American Physical Society. (*c*), (*d*) Reprinted with permission from [47], copyright 2011 by the American Physical Society.

from this assumption, Neupane *et al* calculated the doping evolution of the Lindhard function at the antiferromagnetic wave vector [47]. The result, displayed in figure 7(*b*), shows a surprising similarity with the phase diagram, if we disregard the antiferromagnetic region for reasons mentioned above. For example, the maximum value of the Lindhard function is higher on the hole-doped side than on the electron-doped side, and the position of that maximum is also found at higher doping. Furthermore, the Lindhard function maintains a relatively high value for a wider range of doping in the hole-doped side. Overall, this surprising result suggests some correlation between superconductivity and antiferromagnetic scattering near E_F in the 122-pnictides.

3.4. Other materials

Except for the 122-chalcogenides, which will be described at the end of this section, all Fe-based superconductors share the same fermiology for most of their phase diagram: circular to slightly squarish hole-like FS pockets centred at Γ and a pattern formed by the hybridization of two-ellipse electron-like FS pockets at the antiferromagnetic wave vector M = $(\pi, 0)$. However, the quasi-nesting conditions between these two types of FSs vary from one compound to another. For example, relatively good quasi-nesting is found in the electron-doped 111-pnictide $NaFe_{0.95}Co_{0.05}As$ [57]. In contrast, the quasi-nesting conditions, as defined in section 3.3, are much weaker[5] in SC LiFeAs (T_c = 18 K) [58], even though slightly inelastic antiferromagnetic scattering near the FS remains possible. It is also interesting to point out that all predicted hole-like bands are observed in the 111-pnictides near the Γ point [37, 57, 58] with much less ambiguity than in the 122-pnictides. As with these later materials, the band structure of the 111-pnictides is also renormalized significantly near E_F compared with band structure calculations. A renormalization factor of 3 has been reported for LiFeAs [58] while He *et al* report renormalization by factors varying

[5] We note that Borisenko *et al* use the word 'nesting' in [58] in a much stricter sense than the concept of quasi-nesting defined in section 3.3, and thus claim that there is no nesting at all in LiFeAs.

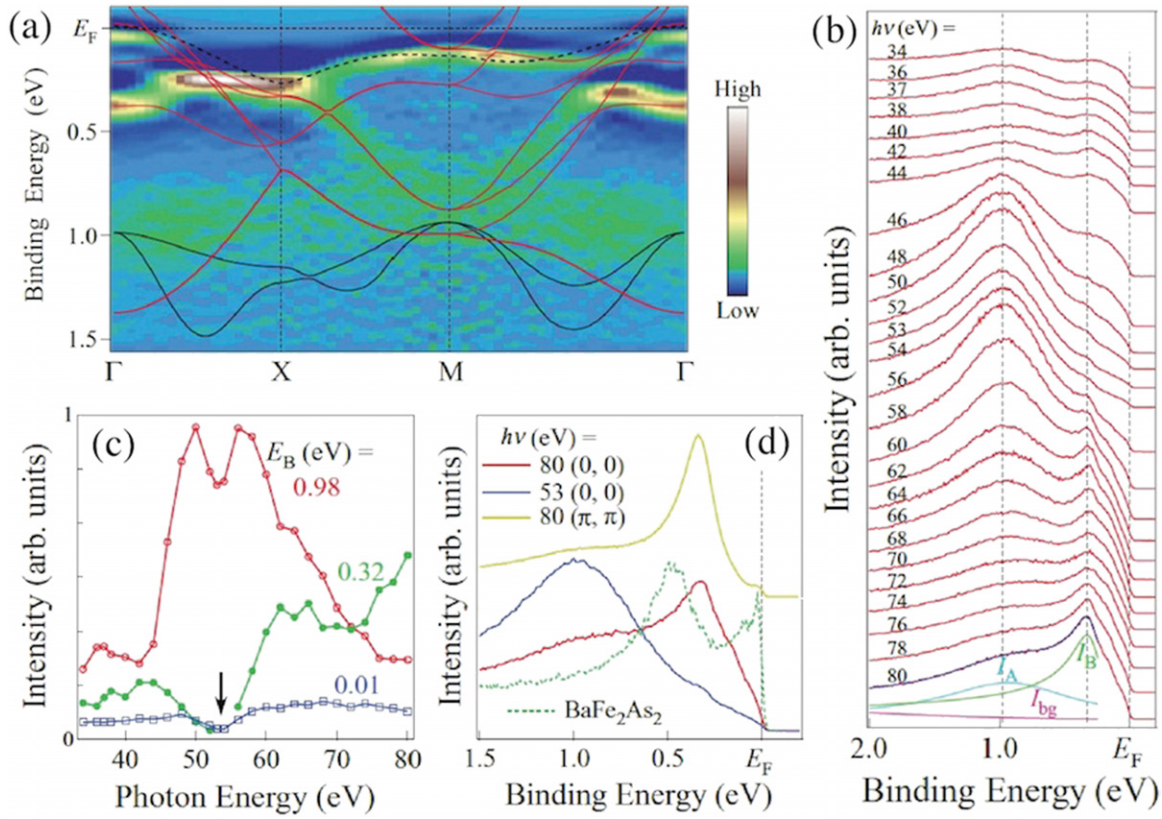

Figure 9. (*a*) Second derivative plot along the Γ–X–M–Γ high-symmetry lines of $Sr_2VFeAsO_3$. LDA + U bands are also plotted for comparison. The Fe3d bands (red/grey lines) are renormalized by a factor of 1.6, whereas the V3d bands (black lines) are not. The Fe3d$_{xy}$ band (black dashed line) is renormalized by a factor of 3.3 to reproduce the experimental band near E_F. (*b*) VB at the BZ centre measured at different photon energies (34–80 eV). All the spectra are normalized by the photon flux. The fitting curves for the spectrum at $h\nu = 80$ eV are also shown. (*c*) Photon energy dependence of the intensities of the two peaks obtained from the fitting curves and the spectral intensity at $E_B = 0.01$ eV. (*d*) Direct comparison of the VB measured at $h\nu = 53$ and 80 eV, along with the VB of $BaFe_2As_2$ ($h\nu = 80$ eV). Reprinted with permission from [63], copyright 2011 by the American Physical Society.

between 4.3 and 5.4 on different bands in the parent compound NaFeAs [37].

Despite an obvious surface problem induced by the absence of an appropriate cleaving plane that results in excess hole doping at the surface layer, ARPES results on the 1111-pnictides [59–62] also indicate essentially the same fermiology as their pnictide cousins. In addition, experimental data indicate a renormalization of the band structure in LaOFeP of 2.2 [59], which is similar to other pnictides. Unlike for other Fe-based superconductors though, no variation of the band structure is observed by ARPES when changing the photon energy [61], which is easily understood since the state probed is a real surface state induced by the cleaving problem for this material.

Among all pnictides, special attention must be devoted to $Sr_2VFeAsO_3$, for which there exists, to our knowledge, only one ARPES report [63]. In addition to Fe3d states, most LDA band calculations predicted the presence of V3d states at the Fermi level that would completely modify the fermiology of this system [64–67]. In fact, one of these papers mentioned that if the FS is derived only from Fe states, it would have a topology comparable to that of the other pnictides [65]. This is precisely what is found experimentally [63]. Using samples smaller than $0.2 \times 0.2\,mm^2$, Qian *et al* determined that the FS of this system is composed of a small and a large Γ-centred hole-like FS (called α and β, respectively) and by electron-like FSs with elongated ellipse shape at the M point. Electron counting from the algebraic FS area leads to a carrier concentration compatible with the Luttinger theorem. Comparing their results with LDA+U calculations, the authors found good agreement with the overall Fe3d band structure when considering a normalization factor of 1.6, as shown in figure 9(*a*). However, the states closer to the Fermi level fit the calculation well only for a renormalization factor of about 3.3 [63]. The main discrepancy between the experimental results and the other LDA calculations relates to the position of the V states. From their resonance profile as a function of incident photon energy, illustrated in figures 9(*b*)–(*d*), the V3d states are found around 1 eV below E_F, a result that is reproduced only when incorporating an effective Hubbard energy U of 6 eV in the LDA + U calculations [63]. It is interesting to note that with V3d electrons in a Mott state and Fe3d electrons at the Fermi level in the absence of Fe–V hybridization, $Sr_2VFeAsO_3$ can be viewed as a perfect orbital selective Mott transition [68, 69] system, such as in $Ca_{1.8}Sr_{0.2}RuO_4$, which has also been characterized by ARPES [70].

The Fe-chalcogenides have been less studied than the pnictides by ARPES, even the 11-chalcogenides that have been synthesized in the early days of Fe-based superconductivity.

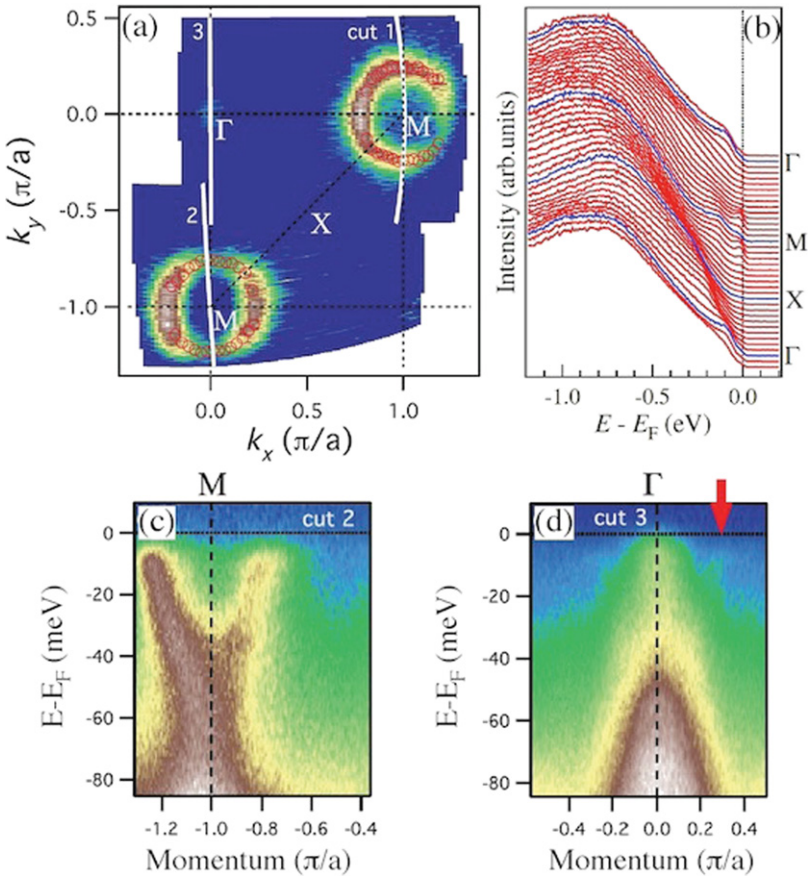

Figure 10. (*a*) Momentum-resolved photoemission intensity mapping of $Tl_{0.63}K_{0.37}Fe_{1.78}Se_2$ recorded in the normal state (35 K) and integrated over a 10 meV window centred at E_F. The small red circles indicate the FS obtained from the MDC peak position at E_F. (*b*) EDCs along several high-symmetry directions in $K_{0.8}Fe_{1.7}Se_2$ recorded with the He I resonance line ($h\nu = 21.218$ eV). Blue (dark grey) curves correspond to high-symmetry points. (*c*) ARPES intensity plot along a cut passing through the M point (cut 1 from (*a*)). (*d*) ARPES intensity plot along a cut passing through the Γ point (cut 3 from (*a*)). (*a*), (*c*), (*d*) Reprinted with permission from [76], copyright 2011 by the European Physical Society. (*b*) Reprinted with permission from [75], copyright 2011 by the American Physical Society.

Nevertheless, existing data of doped 11-chalcogenides show spectral intensity at the Γ and M(π, 0) points [71–73]. Although up to three bands can be identified at Γ, the situation remains more nebulous at the M point, making a careful electron counting analysis difficult. As with pnictides, some high energy features can be well approximated by LDA calculations renormalized by a factor around 2 [71]. However, additional renormalization much stronger than in the pnictides is found near E_F [71, 72], with renormalization factors as large as 20 [72].

Recently, the landscape of Fe-based superconductivity changed abruptly with the discovery of high-T_c (T_c = 29 K) in heavily electron-doped $K_xFe_2Se_2$ [74] and related materials. The input of ARPES to characterize and explain the electronic properties of these materials has been very helpful. Unlike all the other Fe-based superconductors, this system does not show any hole-like FS [75–78], as illustrated in figure 10(*a*). In contrast, a large electron-like FS is observed at the M point. Although the zone centre is free of hole-like FSs, there is evidence for additional electron-like pockets whose origin are not quite clear at the moment. A small 3D electron-like pocket centred at the Z point has been reported in a synchrotron-based study on $A_xFe_2Se_2$ (A = K, Cs) [77]. Traces of these pockets have also been detected in (Tl,K)$Fe_{1.78}Se_2$ [76] and $Tl_{0.58}Rb_{0.42}Fe_2Se_2$ [78] using He discharge lamps. These laboratory-based experiments also reveal an additional electron-like pocket with a size more or less similar to the one centred at the M point [76, 78], as we can see from the comparison of figures 10(*c*) and (*d*).

As with the other Fe-based superconductors, the 122-chalcogenides have their overall band width renormalized by a factor of about 2.5 [75]. What is different though is the energy distribution of the spectral weight, which is closer to the one observed in the cuprates. While the spectral weight of the Fe3d electrons is much larger in the other Fe-based superconductors, the near-E_F bands in $K_{0.8}Fe_{1.7}Se_2$ have much weaker intensity. On the other hand, the intensity of the valence band is more important in these materials. In fact, figure 10(*b*) shows that the weight below 2 eV is concentrated mainly in a broad peak located around 800 meV below E_F, which does not show significant dispersion. That peak, which has been attributed to the incoherent part of the Fe3d states [75], shows an important energy shift at a temperature T^* corresponding to a bump in the resistivity curves [76].

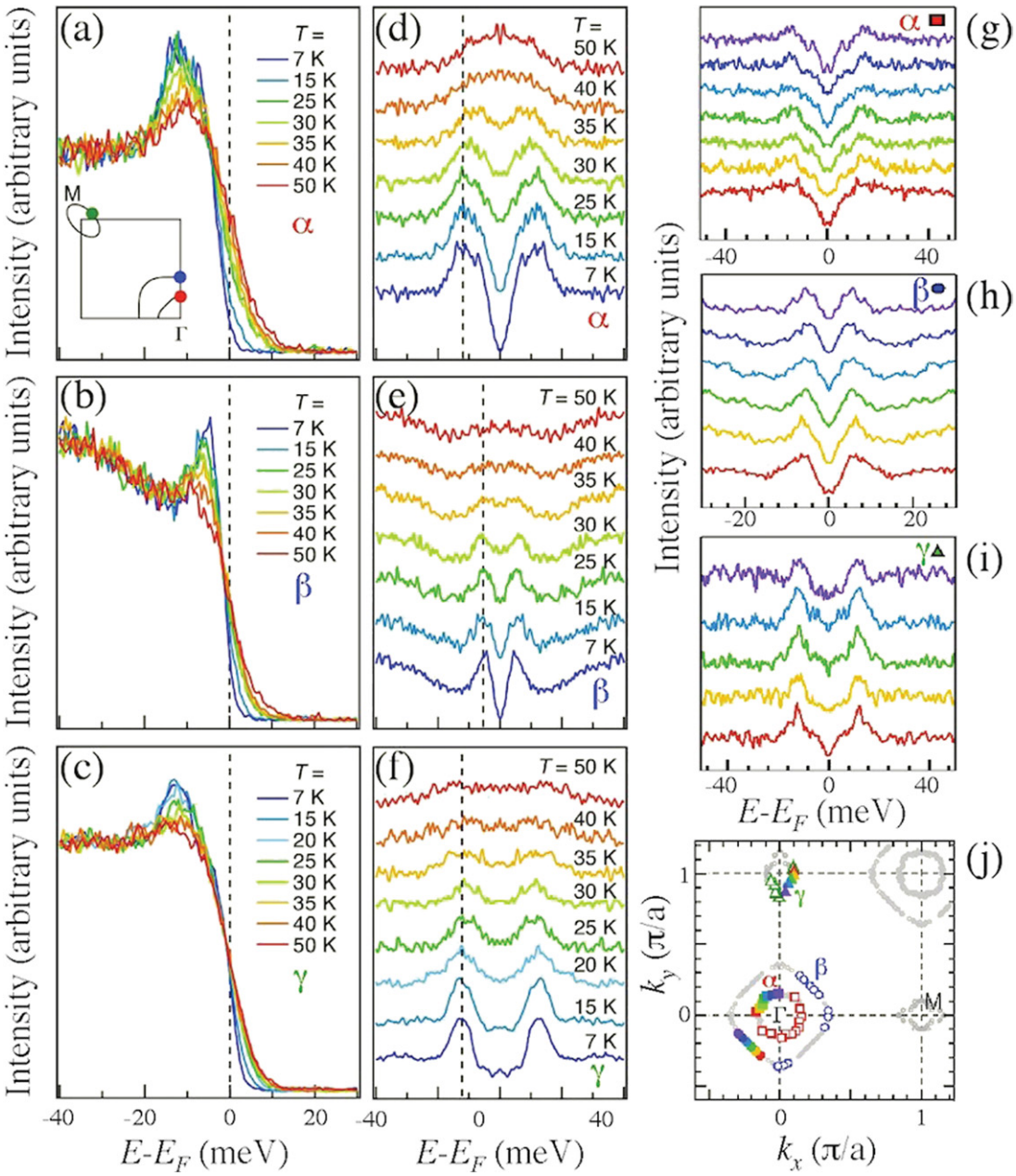

Figure 11. SC gap of $Ba_{0.6}K_{0.4}Fe_2As_2$. (*a*)–(*c*) Temperature dependence of the EDCs on the α, β and δ FSs, respectively. The k_F position of the EDCs is given on the schematic FS (in the 2 Fe/unit cell representation) displayed in the inset of (*a*). (*d*)–(*f*) Corresponding symmetrized EDCs. (*g*)–(*i*) Momentum dependence of symmetrized EDCs at 15 K along the α, β and δ FSs, respectively. The k_F positions are given on the FS displayed in (*j*) in the 1 Fe/unit cell representation. Squares, circles and triangles correspond to the k_F positions on the α, β and δ FSs, respectively. Filled and empty symbols refer to real and symmetrized data, respectively. Adapted from [17], copyright 2008 by the European Physical Society.

4. Superconducting gap

The order parameter describing the SC phase transition is characterized by a complex function represented by the momentum distribution of the gap developing at E_F below the SC critical temperature T_c. The amplitude and phase of the order parameter are directly determined by the electronic structure and by the mechanism responsible for the pairing of charge carriers. Although ARPES is not directly sensitive to the phase, it allows precise measurement of the momentum dependence of the SC gap size, which serves as a powerful tool to validate or invalidate theoretical models. The previous statement is particularly true for multi-band systems, for which the interpretation of transport measurements, which may be momentum-sensitive but not momentum-resolved, becomes difficult or even impossible.

The first ARPES determinations of the SC gap in Fe-based superconductors were obtained on optimally doped $Ba_{0.6}K_{0.4}Fe_2As_2$ [17, 79]. Figures 11(*a*)–(*c*) show the temperature evolution of EDCs from Ding *et al* recorded with the He Iα resonance line on the α, β and γ FSs, respectively [17]. As the temperature decreases below T_c, a coherence

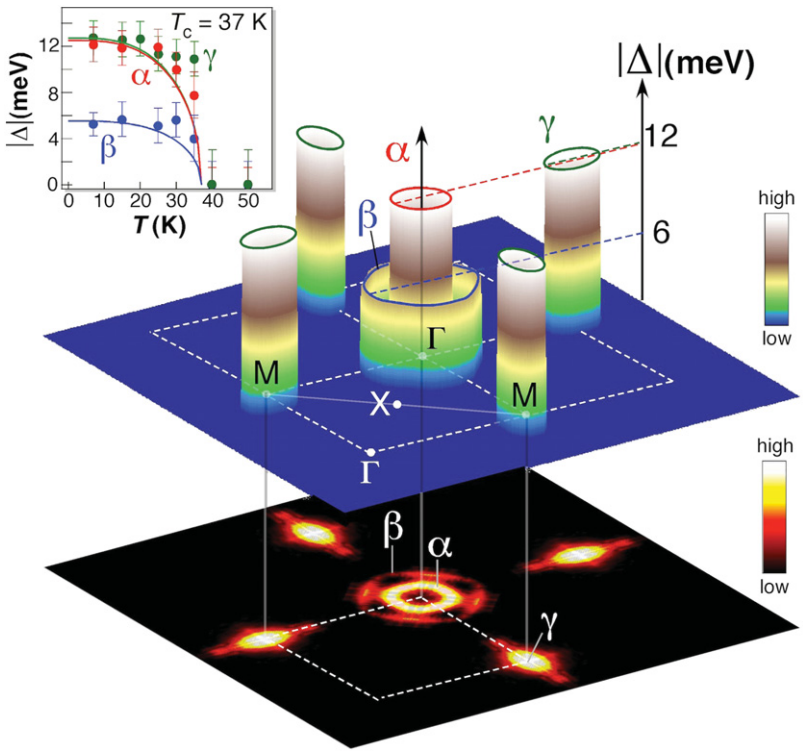

Figure 12. 3D plot of the SC gap size (Δ) measured at 15 K on three FS sheets (shown at the bottom as an intensity plot) and their temperature evolutions (inset). Reprinted with permission from [17], copyright 2008 by the European Physical Society.

peak develops on each FS, indicating the opening of a SC gap, which is better visualized from the corresponding symmetrized EDCs displayed in figures 11(*d*)–(*f*). The full SC gap size 2Δ is given by the distance between the two coherence peaks in the symmetrized EDCs. The SC gap is also characterized by its momentum dependence on each FS, which are shown in figures 11(*g*)–(*i*). The k_F points where these data were collected are indicated in figure 11(*j*).

Figure 12 summarizes the data from Ding *et al* [17]. Unlike the SC gap in the cuprates, these experiments show clearly the absence of nodes along all the FS pockets, ruling out any order parameter with a d-wave symmetry. The invariance of the coherence peak positions in the symmetrized EDCs, shown in figures 11(*g*)–(*i*), and further refined measurements with the He Iα line [18] indicate that the gaps are indeed isotropic. Interestingly though, the gap size is not unique and varies from band to band. More precisely, the gap size is around 12 meV along the quasi-nested FSs, yielding to $2\Delta / k_B T_c$ ratios of about 7.5, while the gap size along the non-quasi-nested β FS pocket drops to 6 meV. We note that although the SC gap seems to disappear above T_c, the temperature evolution of the SC gap size does not follow the Bardeen–Cooper–Schrieffer (BCS) function and shows a much steeper drop while approaching T_c. Isotropic gaps have been reported not only in the 122-pnictides [17, 79], but also in the 111-pnictide [57, 58], the 1111-pnictide [60] and the 11-chalcogenide [71] systems.

To explain these intriguing results, two main models have been proposed for the pairing mechanism: the *FS quasi-nesting model* and the *local antiferromagnetic exchange pairing model*. These two models are radically different. Essentially, the basic question to discriminate one from the other is the following: Does pairing occur due to interactions in the momentum space or in the real space? Historically, the former model gained popularity very quickly, partly due to ARPES results. We thus describe it first, along with the reasons for its initial success, among which are the evidence for the presence of interband scattering in the pnictides and the weakening of the quasi-nesting conditions accompanying the disappearance of superconductivity at very high doping in these materials. Paradoxically, recent ARPES measurements on the 122-chalcogenides are main indicators announcing the dusk of that model to describe the Fe-based superconductors. Nowadays, the local antiferromagnetic exchange pairing model described afterwards appears as a better prospect in claiming for universality of the pairing mechanism in the Fe-based superconductors. Yet the community is still far from ready to unanimously award a laurel wreath to any model candidate.

4.1. Quasi-nesting model

Until the recent discovery of superconductivity in the chalcogenide version of the 122 phase, the quasi-nesting model was the most popular way to account for superconductivity in Fe-based superconductors. The idea is indeed very simple and illustrated in figure 13: when a hole-like FS pocket and an electron-like FS pocket have similar but not exact size and shape, the system can avoid long-range ordered CDW or SDW states but yet maintain important scattering induced by short-range fluctuations through the 'quasi-nesting' wave vector (in this case the antiferromagnetic wave vector) that connects these two FS pockets. Despite the absence of perfect nesting,

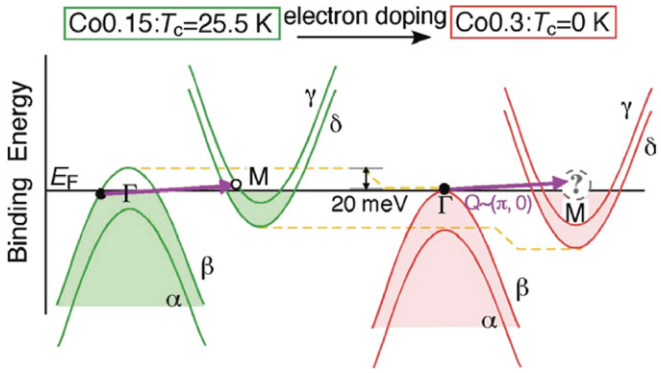

Figure 13. Comparison of energy bands between $BaFe_{1.85}Co_{0.15}As_2$ and $BaFe_{1.7}Co_{0.3}As_2$ samples. The interband scattering is dramatically suppressed in the non-SC $BaFe_{1.7}Co_{0.3}As_2$ compound since the hole-like α and β bands at the Γ point are basically occupied. Reproduced with permission from [54], copyright 2009 by IOP Publishing and Deutsche Physikalische Gesellschaft.

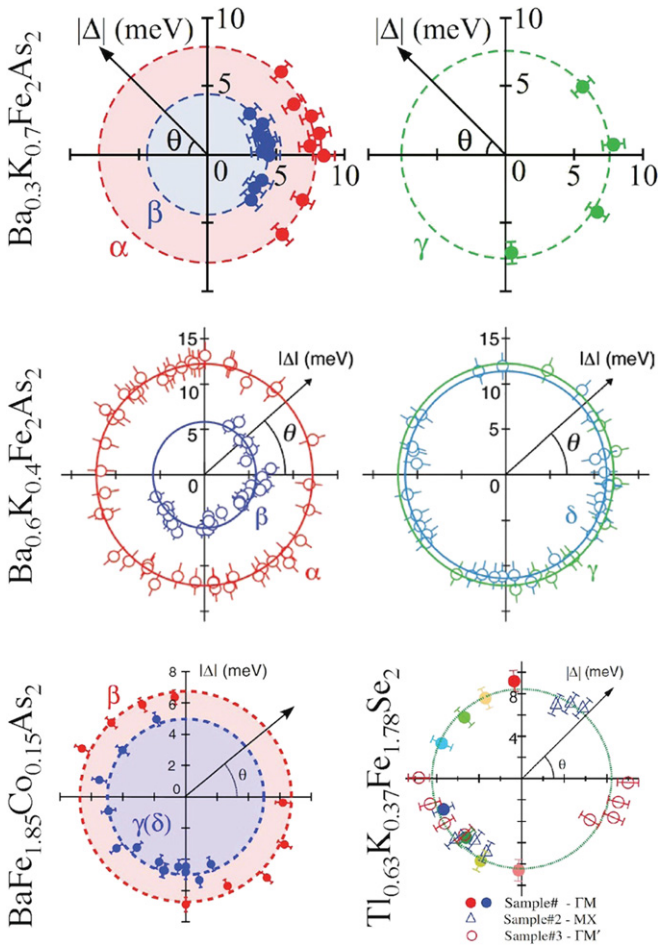

Figure 14. Polar representation of the SC gap amplitude for various bands and materials. The data on $Ba_{0.3}K_{0.7}Fe_2As_2$ are reprinted with permission from [48], copyright 2011 by the American Physical Society. The data on $Ba_{0.6}K_{0.4}Fe_2As_2$ are reprinted with permission from [18], copyright 2009 by the European Physical Society. The data on $BaFe_{1.85}Co_{0.15}As_2$ are from [53], copyright 2009, National Academy of Sciences, USA. The data on $Tl_{0.63}K_{0.37}Fe_2Se_2$ are reprinted with permission from [76], copyright 2011 by the European Physical Society.

a peak of enhanced magnetic susceptibility is still expected at the quasi-nesting wave vector, in which case the kinetic process by which a zero momentum pair formed on one FS is scattered onto another one can be enhanced, thereby increasing the pairing amplitude [17, 80, 81].

In practice, the quasi-nesting model can be tested by checking the evolution of the SC gap size as a function of the quasi-nesting conditions. The latter are easily tuned with doping since the doping evolution of hole-like and electron-like FS pockets with carrier injection has opposite trends. The most drastic effect is observed when extra-doping the system until one type of FS pocket, either electron-like or hole-like, disappears. As mentioned previously, the purely K-substituted 122 compound (KFe_2As_2) is extremely over-hole-doped and does not exhibit any electron-like FS [52]. In agreement with the quasi-nesting model, its T_c drops to a few kelvins only. Unfortunately, the gap size becomes too small to be extracted. Similarly, the disappearance of Γ-centred hole-like FS pockets in heavily electron-doped $BaFe_{1.7}Co_{0.3}As_2$ is accompanied by a total suppression of superconductivity [54]. Another experimental fact consistent with the quasi-nesting model in the 122 system is the switch of the pairing strength on the β band from 'weak coupling' to 'strong coupling' as we compare the optimally-hole doped and optimally-electron doped compounds (see figure 14). While the β FS is larger than the M-centred electron-like FS pockets in the hole-doped compound, its size becomes compatible with the FS pockets at the M point in the optimally-electron doped system, thus promoting antiferromagnetic interband scattering [53].

Whatever it is or not the cause for Fe-based superconductivity, ARPES provides sufficient evidence for interband scattering with the quasi-nesting wave vector. The first piece of evidence is the smaller EDC linewidth of the unnested β band in $Ba_{0.6}K_{0.4}Fe_2As_2$ as compared with the quasi-nested bands [17]. This indicates that the lifetime of the quasi-particles associated with the β band is longer due to the absence of interband scattering. The second piece of evidence is the observation of an anomaly, or *kink*, in the dispersion of bands associated with quasi-nested FS pockets [82]. At 15 K, this anomaly is found around 25 meV, as can been seen from figures 15(*a*)–(*c*). To confirm this result, a self-energy analysis was performed (see figure 15(*e*)) by approximating the bare band dispersion by the dispersion determined at 150 K, way above the critical temperature. This choice of bare band approximation, justified by the absence of the anomaly at 150 K, is critical since the Fe-based superconductors are multi-band systems. In contrast, the cuprates are single-band systems studied not far from half filling, where the band dispersion near E_F can be reasonably well approximated by a straight line. By dividing out the ARPES intensity plot recorded at 150 K by the Fermi–Dirac function, one can reveal the top of the α band about 25 meV above E_F, as illustrated in figure 15(*d*), indicating that the band dispersion in the energy region of the kink is naturally curved and that a straight line cannot be used to approximate the bare band dispersion. In the SC state, both the imaginary and real parts of the self-energy deviate around 25 meV from the quite linear behavior observed at higher energy.

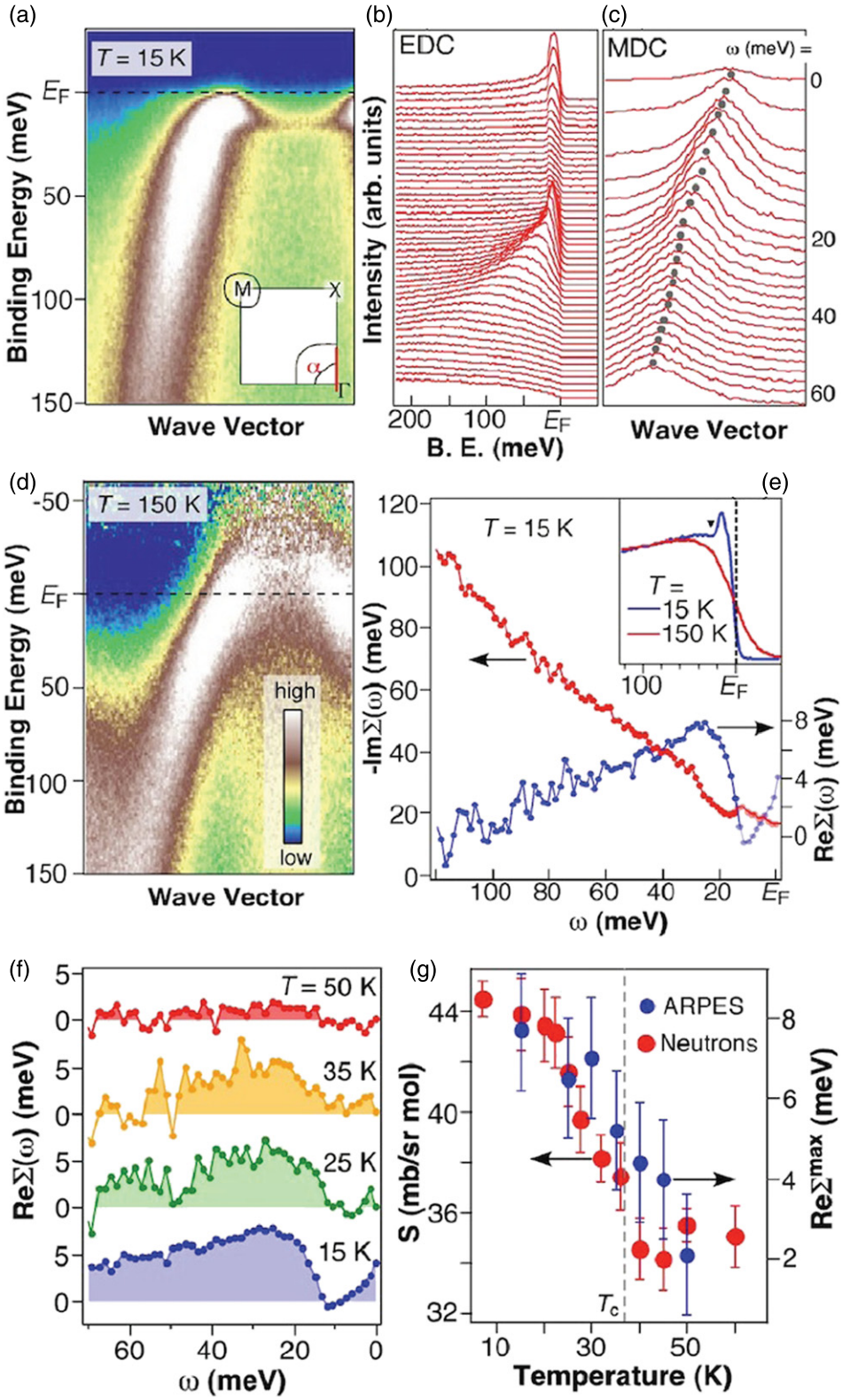

Figure 15. (*a*) ARPES intensity plot in the SC state (15 K) along a cut crossing the α band. The inset shows the schematic FS of $Ba_{0.6}K_{0.4}Fe_2As_2$ with the location of the cut (red) in the 2 Fe/unit cell notation. (*b*) Corresponding EDCs. (*c*) Corresponding MDCs, in the 0–60 meV binding energy range. Grey dots indicate the maximum position of the peaks. (*d*) ARPES intensity plot at 150 K divided by a Fermi–Dirac function, recorded along the same cut as in (*a*). (*e*) Real and imaginary parts of $\Sigma(\omega)$. Fade colours are used for binding energies smaller than 17 meV since $\Sigma(\omega)$ in this range is complicated by particle–hole mixing due to superconductivity. The inset compares the partial DOS along the cuts measured at 15 K (blue) and 150 K (red), respectively. (*f*) Temperature dependence of the real part of the self-energy referred from the MDC fit dispersion at 150 K. (*g*) Maximum value of the real part of the self-energy (blue) plotted as a function of temperature. The ARPES results are compared with the neutron scattering intensity of the 14 meV spin resonance (red) located at the antiferromagnetic wave vector [83]. The dashed line indicates the critical temperature. Reprinted with permission from [82], copyright 2009 by the American Physical Society.

The coupling of an Einstein mode of energy Ω is expected to give rise to an anomaly at $\Omega + \Delta$ [84], where the SC gap Δ is well known for each band. Subtracting the 12 meV energy corresponding to the gap on the α FS from the kink energy yields $\Omega = 13 \pm 2$ meV. While an anomaly is also found in the quasi-nested γ band, the β band shows an anomaly neither at 25 meV nor at 18 meV ($\Delta_\beta + \Omega = 6 + 13$ meV). This band selectivity of the anomaly is in apparent contradiction with a conventional electron–phonon coupling and point toward an electronic origin [82]. Interestingly, the temperature dependence of the kink anomaly, shown in figure 15(f), coincides with the temperature dependence of a spin resonance mode observed by inelastic neutron scattering at 14 meV [83], as illustrated well in figure 15(g). As with the ARPES kink, the spin resonance, detected at the antiferromagnetic wave vector, disappears above T_c, suggesting that the two phenomena are related.

Similarly to the cuprates, antiferromagnetic scattering increases while underdoping Fe-based superconductors [85]. This affects not only the width of the SC quasi-particle peaks, but also their weight. While the SC quasi-particle peak associated with the unnested β band in $Ba_{0.75}K_{0.25}Fe_2As_2$ ($T_c = 26$ K) remains sharp and coherent, the peaks associated with the nested α and γ/δ bands lose their integrity compared with the optimally doped material [49]. Indeed, this dichotomy between the behavior of SC quasi-particle peaks on the unnested and quasi-nested FS pockets upon underdoping is quite similar to the one observed in cuprates between the nodal and antinodal regions. Unlike the quasi-particle peak in the nodal region, the quasi-particle peak at the antinode is suppressed.

At least for the 122-pnictides, which has been more deeply studied, the doping evolution of the quasi-nesting conditions is in qualitative agreement with the variation of T_c. A good illustration of this statement is provided by the doping dependence of the renormalized Lindhard function at the antiferromagnetic wave vector given in figure 8(b), which shows a strong electron–hole asymmetry reflecting the asymmetric band structure with respect to electron or hole doping [47]. While the Lindhard function keeps a high value for a wide hole-doping range before starting to decrease, it decreases monotonically on the electron-doped side, albeit for a small shoulder around $x = 0.24$. Although these calculations performed with the non-magnetic LDA band structure (renormalized by a factor of 4) are not suitable for the antiferromagnetic region near 0 doping, it qualitatively reproduces the size, height and shape of the SC dome away from 0 doping.

Fair agreement with the quasi-nesting model is also obtained for electron-doped $NaFe_{0.95}Co_{0.05}As$ ($T_c = 18$ K), for which Liu *et al* reported almost identical SC gaps (6.8 versus 6.5 meV) on the Γ-centred α' FS pocket and on the M-centred electron FS pockets, which all have similar size [57]. This gap size leads to a $2\Delta/k_BT_c \sim 8$ ratio, indicating that the system is in a strong coupling regime. Using the leading edge shift rather than the SC coherent peak position to identify the gap size, Borisenko *et al* found a $2\Delta/k_BT_c$ ratio of about 3.5 in LiFeAs [58], which is more consistent with the BCS regime. Even though the leading edge method is necessarily an underestimation of the SC gap size, at least by the half-width at half-maximum of the SC coherent peak, LiFeAs shows smaller gap size than $NaFe_{0.95}Co_{0.05}As$. Interestingly, the quasi-nesting conditions are also poorer in LiFeAs, which has one very large and one very small hole-like Γ-centred FS pockets, along with intermediate size M-centred electron-like FS pockets. This reduction of both T_c and the $2\Delta/k_BT_c$ ratio is thus compatible with the quasi-nesting model.

As explained above, LDA calculations predicted the failure of the quasi-nesting model to explain $T_c = 37$ K superconductivity in $Sr_2VFeAsO_3$ [64–67]. The arguments were mainly related to the presence of V states at E_F in the calculated band structure. Although SC gaps were never measured by ARPES due to the small size of the samples, the experimental FS is quite similar to that of the other pnictides and thus consistent with the quasi-nesting scenario [63]. A more intriguing case is that of the 11-chalcogenides. In contrast to the pnictides, the magnetic ground state of their parent compound is not described by the $(\pi, 0)$ wave vector, but rather by a wave vector pointing in the Γ–X direction. Yet, the FS topology of SC 11-chalcogenides is quite similar to that of the pnictides, and ARPES results by Nakayama *et al* suggest that the SC gap of the hole-like band at Γ is also isotropic and in the strong coupling regime [71]. Unfortunately, the low spectral intensity at the M point did not allow the determination of the SC gap there until very recently [73]. In any case, these surprising similarities between SC pnictides and 11-chalcogenides indicate the importance of the $(\pi, 0)$ scattering, even though it does not necessarily prove the validity of the quasi-nesting model in explaining high-T_c superconductivity in these materials. In fact, some neutron scattering experiments suggest that antiferromagnetic scattering at $(\pi, 0)$ is important in this system and even evolves into a resonance for doped samples [86–88].

4.2. Local antiferromagnetic exchange pairing model

Enthusiasm for the quasi-nesting scenario in pnictides was just too strong in the early days to allow the local pairing model to really take off. Nevertheless, Wray *et al* [89] and Nakayama *et al* [18] pointed out that the SC gap measured by ARPES in 122-pnictides is qualitatively consistent with an order parameter that takes the form $\Delta_0 \cos(k_x) \cos(k_y)$. Interestingly, such a formula can be derived from a picture where the pairing occurs in a short distance in real space, for example by considering antiferromagnetic exchange between nearest (J_1) and second-nearest (J_2) neighbors. Figure 16(a) displays the detailed comparison between this formula and the observed gap values obtained by Nakayama *et al* [18]. Apart from small deviations, the same formula applies also to the 111-pnictide $NaFe_{0.95}Co_{0.05}As$, where similar Δ_0 values of 6.8 meV and 6.5 meV are found for the Γ-centred hole-like FS pockets and M-centred electron-like FS pockets, respectively [57].

The presence of a cosine oscillation along the k_z direction of the gap value associated with the α band, illustrated well in figure 16(b) justifies modifications of the

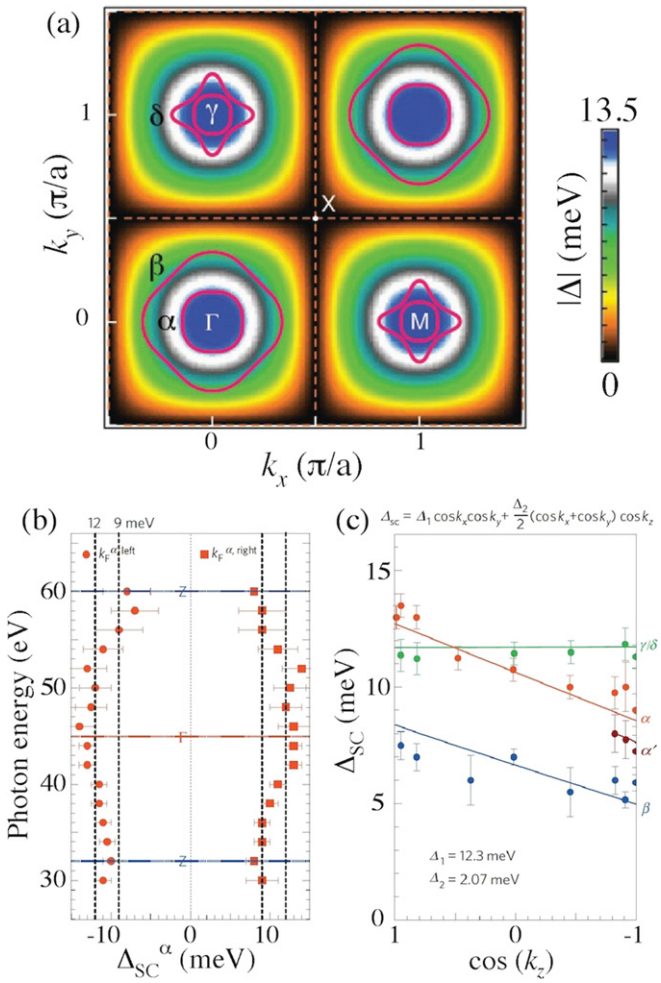

Figure 16. (*a*) Theoretical SC gap value $|\Delta(k) = \Delta_0| \cos k_x \cos k_y|$ with $\Delta_0 = 13.5$ meV as a function of the 2D wave vector [90, 91]. (*b*) Extracted values of the SC gap (defined as the half-value of peak-to-peak positions in the symmetrized EDCs) on the α FS at different photon energies. The dots (squares) are obtained from the left (right) side of k_F on the α FS. (*c*) The SC gap values on the α FS (red dots), β FS (blue dots), γ/δ FS (green dots) and α' FS (brown dots) as functions of the 3D gap function $|\Delta(k_x, k_y, k_z)| = |\Delta_1 \cos k_x \cos k_y + (\Delta/2)(\cos k_x + \cos k_y) \cos k_z|$, with $\Delta_1 = 12.3$ meV and $\Delta_2 = 2.07$ meV, to fit all the SC gaps. The error bars are standard deviations of the measured SC gaps. (*a*) Reproduced with permission from [18], copyright 2009 by the European Physical Society. (*b*), (*c*) Reprinted by permission from Macmillan Publishers Ltd: *Nature Phys.* [19], copyright 2011.

$\Delta = \Delta_0 \cos(k_x) \cos(k_y)$ formula. Xu *et al* [19] started from the simple formula

$$\Delta_{3D}(k_x, k_y, k_z) = \Delta_{2D}(k_x, k_y)(1 + \eta \cos(k_z)) \qquad (4)$$

which is a generalization to layered superconductors of the BCS expression for a superconductor with an isotropic in-plane gap function and where η is a measure of the interlayer coupling strength. With specific considerations applying to the pnictides, they then derived the generalized *s*-wave gap function [19]:

$$\Delta = \Delta_1 \cos(k_x) \cos(k_y) + (\Delta_2/2)(\cos(k_x) + \cos(k_y)) \cos(k_z) + \Delta_3(\cos(k_x) \cos(k_y)) \cos(k_z) \qquad (5)$$

where the gap parameters Δ_1, Δ_2 and Δ_3 can be orbital-dependent or band-dependent in the most general case. Neglecting the last term which is experimentally much smaller than the Δ_2 term due to the vanishingly small η of the M-centred electron-like FS pockets, the experimental data obtained on optimally doped $Ba_{0.6}K_{0.4}Fe_2As_2$ can be fitted well with $\Delta_1 = 12.3$ meV and $\Delta_2 = 2.07$ meV [19]. Figure 16(*c*) shows the fit of SC gap data on all the Fermi surfaces of $Ba_{0.6}K_{0.4}Fe_2As_2$ using a single gap function. Interestingly, the $\Delta_1/\Delta_2 = 5.9$ ratio coincides almost with the $J_{ab}/J_c = 6$ ratio of the in-plane and out-of-plane magnetic coupling constants determined from spin-wave dispersions obtained by neutron scattering experiments on the parent compound [92].

The validity of the gap function given above has been checked for overdoped $Ba_{0.3}K_{0.7}Fe_2As_2$ ($T_c = 22$ K) with the He Iα resonance line (21.218 eV). According to the k_z dispersion of hole-doped 122-pnictides [19], the corresponding photon energy is close to the Γ point, and thus $\cos(k_z) \simeq 1$. The experimental results yield $\Delta_1 = 8.3$ meV and $\Delta_2 = 0.7$ meV [48]. It is worth nothing that within this model the electron-like and the hole-like FS pockets may carry different gaps even if their size is the same since the term $\cos(k_x)+\cos(k_y)$ is 2 and 0 for the Γ and M points, respectively.

Interestingly, the third nearest neighbor antiferromagnetic exchange coupling J_3 in the J_1–J_2–J_3 model is very strong in the chalcogenides and must be taken into account [93]. As a consequence, the formula $|\Delta(k) = \Delta_2| \cos k_x \cos k_y|$ does not apply and must be replaced by $|\Delta(k)| = |\Delta_2 \cos k_x \cos k_y - \Delta_3(\cos 2k_x - \cos 2k_y)/2|$. The latter fits pretty well the data of $FeTe_{0.55}Se_{0.45}$ ($T_c = 14$ K) and the 4.2 meV and 2.6 meV gaps found on the M-centred γ FS and Γ-centred α FS assuming $\Delta_2 = 3.55$ meV and $\Delta_3 = 0.95$ meV [73]. A noticeable feature is the stronger gap at the M point than at the Γ point, which is not the case for the pnictides and that comes out naturally from the J_1–J_2–J_3 model. It also worth mentioning that the Δ_2/Δ_3 ratio is almost the same as the J_2/J_3 ratio determined experimentally from neutron scattering experiments [93].

The revival of the local pairing picture is mainly due to the recent discovery of superconductivity at high temperature in over-electron-doped 122-chalcogenides. As mentioned in section 3.4, these systems are completely free of hole-like FS pockets at the Γ point and thus prevent $(\pi, 0)$ scattering in the electron-hole channel. Unless this new class of materials is the host of a different pairing mechanism, which is quite unlikely due to the structural and electronic similarities between the chalcogenides and the pnictides, the local pairing picture seems more robust as a universal model to explain superconductivity in Fe-based superconductors.

The SC gap of the 122-chalcogenides has been measured for $(Tl,K)Fe_{1.78}Se_2$ [76], $A_xFe_2Se_2$ [77] and $(Tl_{0.58}Rb_{0.42})Fe_{1.78}Se_2$ [78]. All data suggest an isotropic SC around the M-centred electron-like FS pocket. In $Tl_{0.63}K_{0.37}Fe_2Se_2$ ($T_c = 29$ K), a 8.5 meV gap is found, as indicated in figure 14, which leads to $2\Delta/k_BT_c \sim 7$, clearly in the strong coupling limit [76]. SC gaps are also reported for electron-like FSs centred at the Γ point. Hence, Wang *et al* reported a 8 meV for the SC gap on the large

Γ-centred electron-like FS pocket in $Tl_{0.63}K_{0.37}Fe_2Se_2$ [76]. Zhang *et al* reported a 7 meV on the small 3D electron-like pocket centred at the Z point in $K_{0.8}Fe_2Se_2$, as compared with 10.3 meV at the M point [77]. Finally, Mou *et al* recorded a 12 meV gap on the large Γ-centred electron-like FS pocket in $Tl_{0.58}Rb_{0.42}Fe_{1.72}Se_2$ ($T_c = 32$ K), in contrast to the 15 meV SC gap found at the M point [78].

Following the recent developments on the SC gap of the 11-chalcogenides and the 122-chalcogenides as determined from ARPES measurements, the local antiferromagnetic exchange pairing model has been further developed to emphasize not only on the local exchange couplings, but also on the fermiology of the different materials [94]. More precisely, it is argued that high-temperature superconductivity occurs when the FS topology matches the form factor of the pairing symmetry favored by the local antiferromagnetic exchange interactions. The result extends to cuprates as well.

4.3. Temperature dependence of the SC gap

It is has been noticed in an early ARPES report on 122-pnictides that the temperature dependence of the SC gap was not the same as in the BCS superconductors [17]. Unfortunately, the α band shows a 'shoulder' in the SC state that makes a precise characterization difficult. In contrast, the 111-pnictides constitute an ideal system to investigate this issue since no shoulder is observed and the natural cleaved surfaces are expected to be non-polar and free of reconstruction. Liu *et al* performed such a study on electron-doped $NaFe_{0.95}Co_{0.05}As$ [57]. From their data analysis, it is possible to see that the SC gap size Δ, given by half the distance between the two SC coherent peaks, does not change significantly with increasing temperature. Instead, the gap fills up as the temperature increases. A more quantitative approach consists in fitting the experimental EDCs using the self-energy function $\Sigma(k, \omega)$ suggested by Norman *et al* for quasi-particles in the SC state [84]:

$$\Sigma(k, \omega) = -i\Gamma + \frac{\Delta^2}{(\omega + i0^+) + \epsilon(k)} \quad (6)$$

where Γ is the single-particle scattering rate, which is here assumed to be independent of ω. Assuming a polynomial background, this function shows good agreement with the experiments at all temperatures until the SC peak vanishes. As with the scattering rate and the SC gap size, the normalized coherent area Z_A defined as $Z_A = \int A_{coh}(k, \omega)\, d\omega / \int A(k, \omega)\, d\omega$ as in earlier studies on cuprates [95, 96] can also be calculated. While the gap size and the scattering rate seem almost unaffected by temperature, this latter parameter exhibits a significant decrease as temperature increases toward T_c [57]. This result suggests that the unconventional behavior of the SC gap, with the gap filling rather than closing with increasing temperature, is associated with the loss of coherence of the quasi-particle at high temperatures, a characteristic also shared with many cuprates.

4.4. Scaling of the SC gap size with doping

A quite trivial but yet very important remark concerning the SC gap that can be made at least for hole-doped 122-pnictides is the scaling of the SC gap size with T_c as doping varies [18, 49], as verified for all FSs for $T_c \geqslant 22$ K. This result is opposite to the trend reported in some ARPES studies on cuprates and more consistent with recent works suggesting that the SC gap size in underdoped cuprates at the tip of the nodal arc scales with T_c [97]. Essentially, this suggests that the SC gap size is controlled by the pairing amplitude. However, such an observation does not easily extend to the electron-doped side of the 122-pnictides. Indeed, a switch in the pairing amplitude ($2\Delta / k_B T_c$) from the α to the β FSs has been reported [53]. The relative gap amplitude between the β FS and the electron-like FSs at the M point is also different in electron-doped 122-pnictides compared with their hole-doped counterparts. Within the local antiferromagnetic exchange pairing picture, this could be explained by the fact that the gap size is not determined for each FS separately but rather depends on their momentum locations, as defined by global gap parameters determined by local antiferromagnetic exchange constants. In the relatively narrow doping range for which the scaling of the gap size with T_c has been checked, the FS areas vary (and thus the SC gap size) but perhaps not enough to affect the scaling.

4.5. Pseudogap

One of the major problems in the study of cuprates investigated by ARPES is the presence of a pseudogap [98]. Indeed, there is a suppression of DOS near the Fermi level that persists at the antinode up to a temperature T^* which is much higher than T_c. Such behavior is not observed near the nodes. Interestingly, a pseudogap behavior is also observed in $Ba_{0.75}K_{0.25}Fe_2As_2$ [49]. The corresponding feature is detected at 18 meV on the quasi-nested α FS. As shown in figure 17(*a*), the pseudogap feature exhibits some momentum dependence along the α band. While the size of the pseudogap is isotropic, the feature is more pronounced along the Γ–X direction, where the FS topology suggests a stronger antiferromagnetic scattering due to a better quasi-nesting between the α and δ bands, as illustrated in figure 17(*f*). Consistently, the pseudogap is absent on the unnested β FS (see figure 17(*e*)).

As illustrated in figure 17(*a*), the pseudogap is already present in the SC state. With increasing temperature, spectral weight loss is slowly recovered until temperature reaches $T^* = 115$ K, above which no obvious change in the spectrum is detected, as shown in figure 17(*c*). The precise temperature evolution of the spectral weight loss is given in figure 17(*d*).

Combined with the evolution of the spectral lineshape with underdoping, the results of Xu *et al* on $Ba_{1-x}K_xFe_2As_2$ indicate strong similarities with the cuprates that could origin from the importance of antiferromagnetic scattering in these two systems. In particular, the authors can identify two types of regions: (i) regions where there is a smaller SC gap, no pseudogap surviving way above T_c and no loss of integrity of the quasi-particle peak upon underdoping. These regions correspond to the unnested FSs in the Fe-based superconductors and to the nodal region in the cuprates;

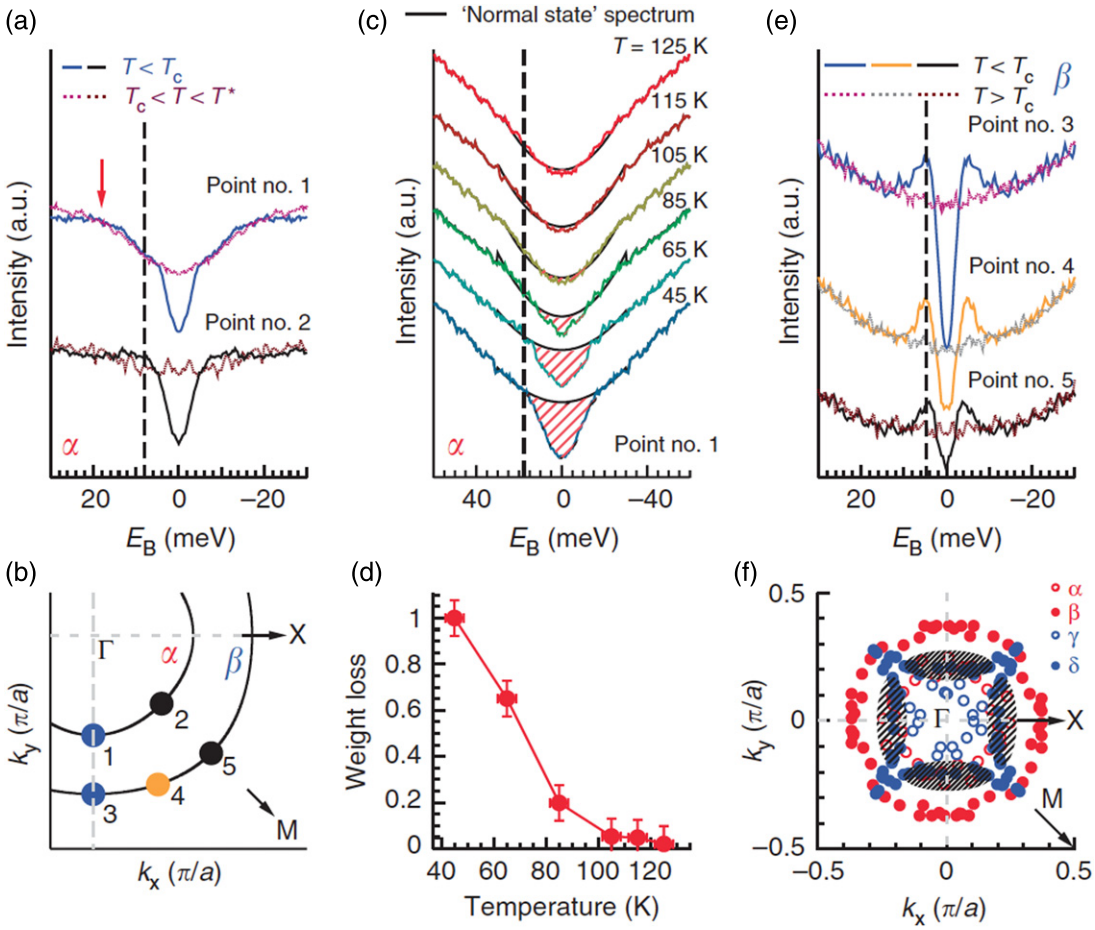

Figure 17. (*a*) Symmetrized EDCs of $Ba_{0.75}K_{0.25}Fe_2As_2$ pnictide measured below and above T_c at two different locations on the α FS (point nos 1 and 2 in (*b*)). The red arrow indicates that the PG is $\sim$ 18 meV, and the dashed vertical line shows that the SC gap on the α FS is $\sim$8 meV. (*b*) Schematic FS plot near the Γ point indicating the measurement locations of spectra presented in (*a*), (*c*) and (*e*). (*c*) T dependence of the symmetrized EDCs of $Ba_{0.75}K_{0.25}Fe_2As_2$ measured at point no. 1 on the α FS above T_c. The vertical dashed line indicates the energy scale of the PG (18 meV). The shaded regions represent the spectral weight loss in the PG state. It is obtained by subtracting the symmetrized EDCs from a quadratic background. (*d*) T dependence of the relative weight loss (normalized by the one obtained at $T = 45$ K) in the PG state of $Ba_{0.75}K_{0.25}Fe_2As_2$. The error bars represent the uncertainty in calculating the relative weight loss. (*e*) Similar to (*a*) but for the β FS (point nos 3, 4 and 5). The dashed line shows the SC gap on the β FS (4 meV). (*f*) Electron-like FS contours of $Ba_{0.75}K_{0.25}Fe_2As_2$ shifted to the Γ point by the antiferromagnetic wave vector. Note that this figure is described in the 2 Fe/unit cell notation. Reprinted by permission from Macmillan Publishers Ltd: *Nature Commun.* [49], copyright 2011.

(ii) regions where the SC gap amplitude is larger and where a pseudogap surviving at high temperatures is found, along with a loss of integrity of the quasi-particle peaks with underdoping. These regions correspond with regions associated with stronger antiferromagnetic scattering, namely the quasi-nested FSs in the Fe-based superconductors and the antinodal region in the cuprates, both of which are connected by the antiferromagnetic wave vector.

5. Discussion

With its ability to *resolve directly* the electronic structure, the FS and the SC gap amplitude in the momentum space, there is no doubt that ARPES is a unique and powerful tool to investigate the electronic properties of multi-band systems such as the Fe-based superconductors. Even though strictly speaking ARPES measures the electronic states in the very few layers below the surface, we presented in this review sufficient consistent results on different crystal structures and cleaved surfaces to prove empirically that ARPES is at the very least a good first-order representation of the electronic states of most bulk Fe-based superconductors. For instance, the momentum dependence observed along the direction perpendicular to the cleaved surface is a strong indication that the probe states are not confined to the surface. Nevertheless, ARPES is not the only experimental technique that can be used to get some insight into the electronic behavior of these materials and at this point we would like to make a comparison regarding the symmetry of the order parameter between ARPES and a bulk transport probe, namely thermal conductivity.

The ARPES results on the SC order parameter are consistent, as suggested by figure 14 for a few materials (we could also include the 111-pnictides [57] and the 11-chalcogenides [71, 73]): (i) the SC gap size is FS dependent; (ii) the SC gap size is in the strong coupling regime, with typical $2\Delta / k_B T_c$ ratios of 5 to 8; (iii) the SC gap size is isotropic or in

the worst case nearly isotropic along each FS taken separately, except perhaps for a small warping along the k_z direction, as observed in optimally doped $Ba_{1-x}K_xFe_2As_2$ [19]. In other words, all the FSs are fully gapped, without any nodes.

It is generally accepted by now that the SC state in the Fe-based superconductors competes with long-range antiferromagnetism. This widespread belief is reinforced by the proximity of the SC and magnetic regimes in the phase diagram. In addition, several theoretical models propose that superconductivity is mediated by short-range antiferromagnetic fluctuations. Consequently, it is very natural to expect that the application of an external magnetic field might not simply suppress superconductivity as in conventional superconductors, but also be accompanied by unwanted secondary effects such as the modulation of the antiferromagnetic fluctuations and the modification of the FS topology. For this simple reason, we prefer to first avoid to compare ARPES with experiments that necessitate the use of an external magnetic field.

Thermal conductivity ($\kappa(T)$) is an experimental probe that does not necessitate the use of an external magnetic field. It usually contains a term linear in temperature that has an electronic origin, and a higher power law term attributed to phonons and other excitations. Near absolute zero temperature, all carriers are paired. Since Cooper pairs cannot carry entropy, the electronic term of the thermal conductivity must vanish, unless some FSs are partly or entirely not gapped, in which case $\kappa(T = 0) \neq 0$. We recall that this condition requires that the samples measured have high quality and are not phase separated. With increasing temperature, quasi-particles thermally excited above the full SC energy gap 2Δ can eventually contribute to the thermal conductivity. Although thermal conductivity does not allow us to directly locate nodes or non-gapped FSs in the momentum space in the case of multiple FS sheets, it is an efficient tool to reveal the existence of such features. It is also important to add that as with ARPES, thermal conductivity in zero field does not rely on any model to claim on the presence of nodes and it is immune to localized states induced by impurities, which is a huge advantage over several other transport techniques that enhances the reliability of the conclusions.

In agreement with the result first demonstrated by ARPES experiments [17, 79], thermal conductivity shows a negligible $\kappa(T \rightarrow 0)/T$ term in optimally doped $Ba_{0.6}K_{0.4}Fe_2As_2$, indicating that all FSs are fully gapped [99]. In fact, that result is still valid down to $x = 0.16$ for in-plane and out-of-plane thermal conductivity in zero field [100], range that extends below the lowest x value for which ARPES measurements have been performed so far. Below that range, Reid *et al* found a sudden increase in the zero field residual $\kappa(T \rightarrow 0)/T$ [100]. It is still debated whether this strange behavior is intrinsic or caused by phase separation at these low dopings. Unfortunately, considering that the gap size becomes small in this region, that the critical temperatures are low compared with typical temperatures used in ARPES and the quasi-particle coherence weakens with underdoping [49], it is unlikely that ARPES can soon provide a definite answer on this issue. It is also not possible for ARPES to check the claim of nodes in the low-T_c compound KFe_2As_2 [101] due to energy resolution and temperature limitations. However, the FS topology measured by ARPES for this system is quite different at the M point from that of the other pnictides [52], and from these results it is conceivable that this particular FS topology leads to a gap structure at the M point that includes nodes and strong anisotropy.

Thermal conductivity measurements were also performed on the electron-doped side of the 122-pnictides. As with their hole-doped counterparts, the electron-doped 122-pnictides exhibit a negligible in-plane $\kappa(T \rightarrow 0)/T$ term [102–104], in agreement with the nodeless SC gaps determined from ARPES measurements [53]. The situation is different for the out-of-plane thermal conductivity, which suggests the presence of nodes [104]. Unfortunately, gap measurements by ARPES have never been reported so far along the k_z direction for the electron-doped 122-pnictides, and a direct comparison is thus impossible. Yet, the ARPES results at a fixed k_z indicate that if there are nodes in $Ba_1Fe_{2-x}Co_xAs_2$, they must be confined to a limited k_z range.

Fe-based superconductors other than the 122-pnictides have also been investigated by thermal conductivity. For instance, Tanatar *et al* measured the in-plane and out-of-plane thermal conductivity of LiFeAs [105]. They find no important residual $\kappa(T \rightarrow 0)/T$ term in zero field, suggesting the absence of nodes in the gap structure, in agreement with ARPES gap measurements in LiFeAs [58] and $NaFe_{0.95}Co_{0.05}As$ [57]. Similarly, Dong and co-workers found only a very small $\kappa(T \rightarrow 0)/T$ residual term in zero field measurements of $FeSe_x$ ($x \sim 1$) by thermal conductivity [106]. The authors conclusion supports multi-gap s-wave superconductivity. Although the sample composition is different from that used by ARPES in Nakayama *et al* [71] and Miao *et al* [73], the results are at least not contradictory.

At this point we can summarize this discussion by saying that whenever ARPES and zero field thermal conductivity data have been recorded under similar conditions, the results are compatible. Now what happens when we add the magnetic field that we deliberately avoided so far to prevent any possible misinterpretation of the experimental data? Unfortunately, the interpretation of thermal conductivity in magnetic field is rarely straightforward for a multi-band system. One can compare the field dependence with that of other materials, but comparisons may be awkward if the systems have different FS topologies, which is typically the case, or if a magnetic ground state competes with superconductivity in some cases and not in the others. Alternatively, one can base his interpretation on theoretical models, with the strong assumption that these models are valid. As a rule of thumb though, it is reasonable to admit that the presence of weak gap states will imprint a fast rising field dependence in the low-temperature thermal conductivity, as these states get more easily excited.

Although no strong SC gap anisotropy is claimed from thermal conductivity measurements in magnetic field on LiFeAs [105] and FeSe [106], the situation is more ambiguous for the 122-pnictides. No strong anisotropy is claimed in $Ba_{0.6}K_{0.4}Fe_2As_2$ for $x > 0.16$, whereas nodes are suggested below that critical doping [100], which has not been

investigated by ARPES. For the electron-doped side, while magnetic field dependent data on $Ba_1Fe_{1.9}Ni_{0.1}As_2$ [102] and underdoped $BaFe_{2-x}Co_xAs_2$ [103] indicate fully or nearly isotropic gaps, the rapid increase in $\kappa(H)$ in the overdoped regime rather suggests a deep gap minimum somewhere on the FS [103].

In the ARPES measurements, the concepts of gap isotropy and gap anisotropy are well defined, the gap being measured directly in the momentum space around each FS taken separately. On the other hand, transport measurements do not have a real momentum resolution. It is possible, for example, to explain the thermal conductivity results in the overdoped regime of $BaFe_{2-x}Co_xAs_2$ by claiming that the gaps around all FSs remain isotropic while one of them, most likely associated with the vanishingly small β FS pocket in this regime, becomes very small in a uniform fashion. Moreover, it worth recalling that unlike ARPES, transport techniques are rather sensitive to the overall gap structure around the BZ centre, and depend not only on the gap size on the various FS sheets, but also on their momentum distribution with respect to the Γ point. Hence, even though ARPES indicates isotropic SC gaps on each FS, the overall SC gap distribution with respect to the Γ point, as measured by ARPES, is anisotropic in the Fe-based superconductors due to the FS topology. In addition, the interactions of the electronic states with an external magnetic field *must* obey selection rules that reflect the point group symmetry of the crystal and that of the overall FS, which is anisotropic.

Before concluding this section, we would like to discuss another possible source of apparent discrepancy between ARPES and some interpretations of transport measurements. As mentioned in this review, the gap Δ in ARPES measurements is usually defined as half of the full gap in the electronic dispersion below the SC transition. This gap is the same one that defines the strength of the pairing interaction, and the same one that characterizes the precise Bogoliubov dispersion below T_c. In that sense, it can arguably be called the 'true gap'. However, the lifetime of the SC quasi-particles in the Fe-based superconductors, characterized by a scattering rate Γ_k, is quite short compared with that of conventional superconductors, which also means that Γ_k is large. Consequently, there is an in-gap residual DOS whose extension may be roughly represented by the leading edge position $\delta_{LE}(k)$ of the ARPES EDCs. Assuming infinite resolution and neglecting thermal broadening, $\delta_{LE}(k) = \Delta - \Gamma_k$, which illustrates that the leading edge is necessarily an underestimation of the 'true gap' size. If ever transport measurements were sensitive to this residual DOS near E_F, the symmetry of the order parameter determined by these techniques would reflect the symmetry of $\delta_{LE}(k)$ rather than that of the 'true gap'. Since Γ_k is momentum-dependent and depends, for instance, on the nearly elastic components of the antiferromagnetic scattering, we should expect a non-negligible momentum dependence for $\delta_{LE}(k)$, especially in the presence of an applied magnetic field.

6. Conclusion

As compared with the high-T_c cuprates, the progress of our understanding of the ARPES measurements on Fe-based superconductors during the past 4 years has been extremely fast. Interestingly, there is also much less discrepancy found in the literature among work from different groups. Even though there is still no consensus on the nature of superconductivity in these materials, the contribution to the current knowledge provided by ARPES is significant and includes the precise determination of the FS topology of different compounds, the observation of electronic renormalization and band dispersion anomalies, as well as the characterization of the size and the symmetry of the SC order parameter. Thus, we can draw some very important conclusions among which are the following: (i) the FS of the Fe-based superconductors is composed of several FS pockets; (ii) the electronic dispersion of these materials is more 3D than most copper oxide superconductors; (iii) the band structure exhibits a non-negligible renormalization compared with LDA calculations that is more pronounced for the low-energy states near the Fermi level; (iv) the SC gap of these materials is FS sheet dependent but isotropic or nearly isotropic on each FS; (v) the pairing strength determined from the SC gap size indicates a pairing in the strong coupling regime; (vi) antiferromagnetic scattering plays an important role in these materials. Furthermore, we provided evidence for consistency between ARPES and other types of measurements. Hopefully, the accumulation of experimental data from ARPES and other probes will soon pave the way to a global understanding of the key features leading to the exotic electronic behavior of Fe-based superconductors.

Acknowledgments

PR and HD are thankful to the Chinese Academy of Sciences (grant No 2010Y1JB6), the Ministry of Science and Technology of China (grant Nos 2010CB923000 and 2011CBA00101), and the Nature Science Foundation of China (grant Nos 10974175, 11004232 and 11050110422). TS, KN and TT are also thankful to the MEXT of Japan, JSPS and TRIP-JST.

References

[1] Kamihara Y, Watanabe T, Hirano M and Hosono H 2008 *J. Am. Chem. Soc.* **130** 3296
[2] Johnston D C 2010 *Adv. Phys.* **59** 803
[3] Gasparov V A 2010 *J. Exp. Theor. Phys.* **111** 313
[4] Paglione J and Greene R L 2010 *Nature Phys.* **6** 645
[5] Stewart G R 2011 arXiv:1106.1618v1
[6] Lumsden M D and Christianson A D 2010 *J. Phys.: Condens. Matter* **22** 203203
[7] Mizuguchi Y and Takano Y 2010 *J. Phys. Soc. Japan* **79** 102001
[8] Kiss T *et al* 2005 *Phys. Rev. Lett.* **94** 057001
[9] Souma S, Sato T, Takahashi T and Baltzer P 2007 *Rev. Sci. Instrum.* **78** 123104
[10] Kamakura N, Takata Y, Tokushima T, Harada Y, Chainani A, Kobayashi K and Shin S 2004 *Europhys. Lett.* **67** 240

[11] Hsieh D, Xia Y, Wray L, Qian D, Gomes K K, Yazdani A, Chen G F, Luo J L, Wang N L and Hasan M Z 2008 arXiv:0812.2289v1
[12] Nascimento V B *et al* 2009 *Phys. Rev. Lett.* **103** 076104
[13] Ding H *et al* 2011 *J. Phys.: Condens. Matter* **23** 135501
[14] Lad R J and Henrich V E 1989 *Phys. Rev.* B **39** 13478
[15] Ma F, Lu Z and Xiang T 2010 *Front. Phys. China* **5** 150
[16] Xu G, Zhang H J, Dai X and Fang Z 2008 *Europhys. Lett.* **84** 67015
[17] Ding H *et al* 2008 *Europhys. Lett.* **83** 47001
[18] Nakayama K *et al* 2009 *Europhys. Lett.* **85** 67002
[19] Xu Y-M *et al* 2011 *Nature Phys.* **7** 198
[20] Zhang Y *et al* 2010 *Phys. Rev. Lett.* **105** 117003
[21] Valla T, Fedorov A V, Johnson P D, Wells B O, Hulbert S L, Li Q, Gu G D and Koshizuka N 1999 *Science* **285** 2110
[22] Yang H-B *et al* 2005 *Phys. Rev. Lett.* **95** 146401
[23] Vilmercati P *et al* 2009 *Phys. Rev.* B **79** 220503(R)
[24] Liu C *et al* 2009 *Phys. Rev. Lett.* **102** 167004
[25] Richard P *et al* 2010 *Phys. Rev. Lett.* **104** 137001
[26] Fink J *et al* 2009 *Phys. Rev.* B **79** 155118
[27] Malaeb W *et al* 2009 *J. Phys. Soc. Japan* **78** 123706
[28] Yi M *et al* 2009 *Phys. Rev.* B **80** 174510
[29] Yang L X *et al* 2009 *Phys. Rev. Lett.* **102** 107002
[30] Liu G *et al* 2009 *Phys. Rev.* B **80** 134519
[31] Brouet V, Marsi M, Mansart B, Nicolaou A, Taleb-Ibrahimi A, Le Fèvre P, Bertran F, Rullier-Albenque F, Forget A and Colson D 2009 *Phys. Rev.* B **80** 165115
[32] Kondo T *et al* 2010 *Phys. Rev.* B **81** 060507(R)
[33] Yi M *et al* 2011 *Proc. Natl Acad. Sci. USA* **108** 6878
[34] Kim Y *et al* 2011 *Phys. Rev.* B **83** 064509
[35] Xia Y, Qian D, Wray L, Hsieh D, Chen G F, Luo J L, Wang N L and Hasan M Z 2009 *Phys. Rev. Lett.* **103** 037002
[36] Zhang Y *et al* 2010 *Phys. Rev.* B **82** 165113
[37] He C *et al* 2010 *Phys. Rev. Lett.* **105** 117002
[38] Harrison N and Sebastian S E 2009 *Phys. Rev.* B **80** 224512
[39] Sebastian S E, Gillett J, Harrison N, Lau P H C, Singh D J, Mielke C H and Lonzarich G G 2008 *J. Phys.: Condens. Matter* **20** 422203
[40] Analytis J G, McDonald R D, Chu J-H, Riggs S C, Bangura A F, Kucharczyk C, Johannes M and Fisher I R 2009 *Phys. Rev.* B **80** 064507
[41] Ran Y, Wang F, Zhai H, Vishwanath A and Lee D-H 2009 *Phys. Rev.* B **79** 014505
[42] Hu W Z, Dong J, Li G, ZHeng P, Chen G F, Luo J L and Wang N L 2008 *Phys. Rev. Lett.* **101** 257005
[43] Hassan M Z and Bernevig B A 2010 *Physics* **3** 27
[44] Yin Z P, Haule K and Kotliar G 2011 *Nature Phys.* **7** 294
[45] Rotter M, Pangerl M, Tegel M and Johrendt D 2008 *Angew. Chem. Int. Edn Engl.* **47** 7949
[46] Pratt D K, Tian W, Kreyssig A, Zarestky J L, Nandi S, Ni N, Bud'ko S L, Canfield P C, Goldman A I and McQueeney R J 2009 *Phys. Rev. Lett* **103** 087001
[47] Neupane M *et al* 2011 *Phys. Rev.* B **83** 094522
[48] Nakayama K *et al* 2011 *Phys. Rev.* B **83** 020501(R)
[49] Xu Y-M *et al* 2011 *Nature Commun.* **2** 392
[50] Cvetkovic V and Tesanovic Z 2009 *Europhys. Lett.* **85** 37002
[51] Wang F, Zhai H and Lee D-H 2009 *Europhys. Lett.* **85** 37005
[52] Sato T *et al* 2009 *Phys. Rev. Lett.* **103** 047002
[53] Terashima K *et al* 2009 *Proc. Natl Acad. Sci. USA* **106** 7330
[54] Sekiba Y *et al* 2009 *New J. Phys.* **11** 025020
[55] Liu C *et al* 2010 *Nature Phys.* **6** 419
[56] Wadati H, Elfimov I and Sawatzky G A 2010 *Phys. Rev. Lett.* **105** 157004
[57] Liu Z-H *et al* 2011 *Phys. Rev.* B **84** 064519
[58] Borisenko S V *et al* 2010 *Phys. Rev. Lett.* **105** 067002
[59] Lu D H *et al* 2008 *Nature* **455** 81
[60] Kondo T *et al* 2008 *Phys. Rev. Lett.* **101** 147003
[61] Liu C, Lee Y, Palczewski A D, Yan J-Q, Kondo T, Harmon B N, McCallum R W, Lograsso T A and Kaminski A 2010 *Phys. Rev.* B **82** 075135
[62] Liu H *et al* 2010 *Phys. Rev. Lett.* **105** 027001
[63] Qian T *et al* 2011 *Phys. Rev.* B **83** 140513(R)
[64] Lee K-W and Pickett W E 2010 *Europhys. Lett.* **89** 57008
[65] Mazin I I 2010 *Phys. Rev.* B **81** 020507(R)
[66] Shein I R and Ivanovskii A L 2009 *J. Supercond. Nov. Magn.* **22** 613
[67] Wang G, Zhang M, Zheng L and Yang Z 2009 *Phys. Rev.* B **80** 184501
[68] Anisimov V I, Nekrasov I A, Kondakov D E, Rice T M and Sigrist M 2002 *Eur. Phys. J.* B **25** 191
[69] Liebsch A 2003 *Phys. Rev. Lett.* **91** 226401
[70] Neupane M, Richard P, Pan Z-H, Xu Y-M, Jin R, Mandrus D, Dai X, Fang Z, Wang Z and Ding H 2009 *Phys. Rev. Lett.* **103** 097001
[71] Nakayama K *et al* 2010 *Phys. Rev. Lett.* **105** 197001
[72] Tamai A *et al* 2010 *Phys. Rev. Lett.* **104** 097002
[73] Miao H *et al* 2011 arXiv:1107.0985v1
[74] Guo J, Jin S, Wang G, Wang S, Zhu K, Zhou T, He M and Chen X 2010 *Phys. Rev.* B **82** 180520(R)
[75] Qian T *et al* 2011 *Phys. Rev. Lett.* **106** 187001
[76] Wang X-P, Qian T, Richard P, Zhang P, Dong J, Wang H-D, Dong C-H, Fang M-H and Ding H 2011 *Europhys. Lett.* **93** 57001
[77] Zhang Y *et al* 2011 *Nature Mater.* **10** 273
[78] Mou D *et al* 2011 *Phys. Rev. Lett.* **106** 107001
[79] Zhao L *et al* 2008 *Chin. Phys. Lett.* **25** 4402
[80] Mazin I I and Schmalian J 2009 *Physica* C **469** 614
[81] Graser S, Maier T A, Hirschfeld P J and Scalapino D J 2009 *New J. Phys.* **11** 025016
[82] Richard P, Sato T, Nakayama K, Souma S, Takahashi T, Xu Y-M, Chen G F, Luo J L, Wang N L and Ding H 2009 *Phys. Rev. Lett.* **102** 047003
[83] Christianson A D *et al* 2008 *Nature* **456** 930
[84] Norman M R and Ding H 1998 *Phys. Rev.* B **57** 11089(R)
[85] Ning F L, Ahilan K, Imai T, Sefat A S, McGuire M A, Sales B C, Mandrus D, Cheng P, Shen B and Wen H-H 2010 *Phys. Rev. Lett.* **104** 037001
[86] Iikubo S, Fujita M, Niitaka S and Takagi H 2009 *J. Phys. Soc. Japan* **78** 103704
[87] Qiu Y *et al* 2009 *Phys. Rev. Lett.* **103** 067008
[88] Liu T J *et al* 2010 *Nature Mater.* **9** 716
[89] Wray L *et al* 2008 *Phys. Rev.* B **78** 184508
[90] Seo K, Bernevig B A and Hu J 2008 *Phys. Rev. Lett.* **101** 206404
[91] Korshunov M M and Eremin I 2008 *Phys. Rev.* B **78** 140509(R)
[92] Zhao J *et al* 2008 *Phys. Rev. Lett.* **101** 167203
[93] Lipscombe O J, Chen G F, Fang C, Perring T G, Abernathy D L, Christianson A D, Egami T, Wang N L, Hu J and Dai P 2011 *Phys. Rev. Lett.* **106** 057004
[94] Hu J and Ding H 2011 arXiv:1107.1334v1
[95] Ding H, Engelbrecht J R, Wang Z, Campuzano J C, Wang S-C, Yang H-B, Rogan R, Takahashi T, Kadowaki K and Hinks D G 2001 *Phys. Rev. Lett.* **87** 227001
[96] Feng D L *et al* 2000 *Science* **289** 277
[97] Hufner S, Hossain M A, Damascelli A and Sawatzky G A 2008 *Rep. Prog. Phys.* **71** 062501
[98] Ding H, Yokoya T, Campuzano J C, Takahashi T, Randeria M, Norman M R, Mochiku T, Kadowaki K and Giapintzakis J 1996 *Nature* **382** 51
[99] Luo X G *et al* 2009 *Phys. Rev.* B **80** 140503(R)
[100] Reid J-Ph *et al* 2011 arXiv:1105.2232v1
[101] Dong J K, Zhou S Y, Guan T Y, Zhang H, Dai Y F, Qiu X, Wang X F, He Y, Chen X H and Li S Y 2010 *Phys. Rev. Lett.* **104** 087005

[102] Ding L *et al* 2009 *New J. Phys.* **11** 093018
[103] Tanatar M A, Reid J-Ph, Shakeripour H, Luo X G, Doiron-Leyraud N, Ni N, Bud'ko S L, Canfield P C, Prozorov R and Taillefer L 2010 *Phys. Rev. Lett.* **104** 067002
[104] Reid J-Ph, Tanatar M A, Luo X G, Shakeripour H, Doiron-Leyraud N, Ni N, Bud'ko S L, Canfield P C, Prozorov R and Taillefer L 2010 *Phys. Rev.* B **82** 064501
[105] Tanatar M A *et al* 2011 arXiv:1104.2209v2
[106] Dong J K, Guan T Y, Zhou S Y, Qiu X, Ding L, Zhang C, Patel U, Xiao Z L and Li S Y 2009 *Phys. Rev.* B **80** 024518